DEVELOPING AGED AND UNAGED MICRO AND NANOPLASTICS FOR ENVIRONMENTAL TESTING

by

Elnaz Kalantar

A thesis submitted in partial fulfillment of the requirements for the degree of

Master of Science

in

Environmental Science

Department of Civil and Environmental Engineering

University of Alberta

Abstract

Concerns are growing about plastics in the environment. The aging of the plastics in the environment will impact their fate and their interactions with the ecosystems' constituents. As such, there is a need to improve our understanding of aged plastics and how they differ from their pristine or primary counterparts. Toward this aim, this work details the formation of primary and secondary polystyrene (PS) micro and nanoplastics (MNPs) and their weathering by a combination of UV light, heat, and mechanical abrasion.

Primary MNPs were produced through the dissolution of PS in chloroform followed by anti-solvent precipitation in a 10% polyvinyl alcohol (PVA) solution. Secondary MNPs were produced through mechanical abrasion and shear stresses using a ball mill grinder. Following production, particles were filtered, purified, and concentrated in a deionized water (DI) suspension. Weathering of primary and secondary MNPs was performed by Ultraviolet (UV) light exposure to produce surface oxidation, as confirmed by Fourier transform infrared spectroscopy (FTIR).

Characterization of MNPs was performed by scanning electron microscopy (SEM), Coulter counter, laser diffraction, dynamic light scattering (DLS), electrophoretic mobility, and FTIR analyses. Both primary and secondary MNP suspensions had an average particle size in nano-scale (~ 330 ± 2 nm and 155.7 ± 1.5 nm, respectively), though SEM indicated primary MNPs were spherical while secondary MNPs were irregularly shaped. Chemical characterization of primary and secondary MNPs showed the same PS signature of the parent material, and oxidation due to UV light and heat exposure in weathered MNPs was monitored by FTIR.

Due to changes in morphology and surface chemistry, secondary and weathered MNPs are anticipated to behave differently from primary particles. Comparing primary to secondary and

weathered MNPs will determine the dependence of aging on particle behavior and will improve the applicability of lab-scale testing when seeking to understand environmental impacts.

Preface

Chapter 1 provides a brief introduction to the need for relevant research, references the gaps regarding this topic, and states the goals of this paper. Chapter 2 includes background information (i.e., related fundamental scientific concepts), and defining technical words. In addition, it covers previous studies related to this work. Chapter 3 contains the detailed methodology, techniques, and instruments used in this thesis. Chapter 4 provides the obtained data in this study and discusses and analyzes them. Chapter 5 introduces the ongoing studies as well as some recommendations for future works regarding this thesis and summarizes the conclusion of this thesis considering this paper's goals. Chapter 6 includes a list of references used in this thesis.

Dedication

To my beloved people in my life:

I dedicate this to my late father (Homayoun Kalantar) who taught me diligence.

I dedicate this to my late grandmother (Delaram Rostami) who loved me unconditionally.

I dedicate this to my mother (Mina Rasaei) who has been providing me with peace, and love…

I dedicate this to my brother (Amirhossein Kalantar) who has been supporting me.

I dedicate this to my sister-in-law (Anahita Shareghi) and her kids (Artemis Kalantar, and Arta Kalantar) who have brought happiness to my life.

I dedicate this to my uncle (Nader Rassaei) who taught me humanity and unconditional generosity.

I dedicate this to my cousin (Reza Nasseri) who taught me kindness.

I dedicate this to my life friend (Matthew Scott Macneil) who has given me confidence and supported me in all aspects of this journey.

Acknowledgment

First of all, I would like to thank my esteemed supervisor, Dr. Jeffrey Farner, for providing me with guidance, and support and teaching and supervising me patiently. He encouraged me always during this journey and by his understanding he taught me not to be scarred by my mistakes but to learn from them. It was my honor to know him and work under his supervision. I am grateful for everything learned from him both the academical knowledge and humanity lessons.

My deepest appreciation goes to Dr. Greg Goss for supporting me with his knowledge and providing me with the lab equipment used in this study.

I would like to acknowledge Dr. Ratmir Derda and Dr. Jonathan Veinot for sharing their lab facilities and equipment.

In the end, I would like to thank my friends at the University of Alberta, Dr. Sina Neshati, Dr. Foroogh Mehravaran, Dr. Sina Esfandiari, Dr. Wafa Dastyar, Dr. Yueyang Zhang, and Afrida Nurain who eased this journey with their support.

Table of Contents

List of Tables

List of Figures

Abbreviations and Units

kg	kilogram
mm	millimetre
nm	nanometre
µm	micrometre
PE	polyethylene
PP	polypropylene
PET	polyethylene terephthalate
PS	polystyrene
PVC	polyvinyl chloride
UV	Ultraviolet
MPs	microplastics
NPs	nanoplastics
MNPs	micro and nanoplastics
ABS	acrylonitrile, butadiene, and styrene
Molecular weight	molecular weight
g/mol	gram per mole
°C	Celsius
T_g	glass transition temperature
g/cm^3	gram per cubic metre
EC	European Commission
USEPA	US Environmental Protection Agency
FDA	US Food and Drug Administration
OSHA	Occupational Safety and Health Administration
CPSC	Consumer Product Safety Commission
EPAS	evaporative precipitation into an aqueous solution
LAS	liquid anti-solvent precipitation
$C_{nucleation}$	The concentration at which nucleation occurs
$C_{solubility}$	equilibrium concentration
PVA	polyvinyl alcohol
SDS	sodium dodecyl sulfate
CUR	curcumin
COU	coumarin 6
NOR	nortriptyline hydrochloride
AMI	amitriptyline
PRO	prochlorperazine dimeleate
mL/min	millilitre per minute
rpm	round per minute
LDPE	low-density polyethylene
THF	tetrahydrofuran

PVP	polyvinylpyrrolidone
EtOH	ethanol
AC	acetone
PA	polyamide
HDPE	high density polyethylene
PD	polydispersity
MQW	Mili-Q water
mg	milligram
mg/mL	milligram per millilitre
HPLC	high-performance liquid chromatography
mL	millilitre
g	gram
G	gauge
TOC	total organic carbon
mgC/L	mg of carbon per litre
µm	microlitre
Min	minimum
min	minute
K	Kelvin
W	Watt
$\mu W/cm^2$	microwatt per square centimeter
-OH	hydroxyl group
$-CH_3$	methyl group
Au/Pd	gold/palladium
DLS	dynamic light scattering
NaCl	sodium chloride
n	number
Wt%	weight percentage
Dv	volume weighted diameter
Dn	number weighted diameter
PDI	polydispersity index
mV	millivolt
Z-ave	zeta average
Z-average	zeta average
d	diameter
SEM	scanning electron microscopy
kV	kilovolt
FTIR	Fourier transform infrared spectroscopy
cm^{-1}	one per centimeter
C=C	double bond carbon/carbon
-C-O	single bond carbon/oxygen (alkoxy group)
$-CH_2$	methylene group

C-C	single bond carbon/carbon
C-H	single bond carbon/hydrogen
C-O-C	ether group
C-O-O-H	hydroperoxide group
C-OH	phenolic hydroxyl group
UV-Vis	UV-Visible
μ-FTIR	micro-Fourier transform infrared
W-PE	weathered polyethylene
N-PE	nonweathered polyethylene
M_n	number-average molecular weight
Nano-AFMIR	infrared spectroscopy coupled to atomic force microscopy

Chapter 1: Introduction

Plastic pollution is a growing concern worldwide [1]. Significant plastic consumption, as well as mismanagement of plastic debris, has resulted in them becoming a ubiquitous contaminant in different ecosystems, especially in aquatic ones [2, 3]. Annually, more than 3×10^{11} kg of plastics are manufactured, and it is forecasted to be increased almost twice in the next 20 years [3, 4]. Therefore, plastic waste has become one of the major environmental concerns in the past five decades [5].

Produced plastic commonly are polyethylene (PE), polypropylene (PP), polyethylene terephthalate (PET), polystyrene (PS), and polyvinyl chloride (PVC) [4, 6, 7]. Plastics have many applications including the manufacture of single-use plastics (e.g., plastic packaging, plastic bottles), and cosmetic products [8-10]. In the last 50 years, plastic waste has risen to around 8.7% yearly [5]. For instance, almost 63×10^5 kg of plastic waste was produced in 2015, but only 9% was recycled, and the rest was either incineration or in landfills and the environment [11].

It has been estimated that 11% of the plastic waste ends in aquatic ecosystems [8]. The common plastic litter found in the surface layer of aquatic systems and shore-lines is PE and PP waste, while in sewage treatment works, and deep-sea sediments PS and cellulosic fibres are the main plastic [12].

The durability of plastics is due to their non-biodegradability, so they may remain in the environment for centuries after introduction [13]. Larger plastic pieces are aged due to aging factors in the environment (i.e., ultraviolet (UV) radiation, mechanical forces, and biological activities). The aging process causes the fractures of them into smaller fragments, i.e., microplastic (MPs,), and nanoplastics (NPs) [1]. The size range of MPs commonly is defined from 0.1mm to

5 mm, while NPs' size range is considered from 1nm to 1 μm [14]. Weathering of the plastics leads to modification of their physiochemical properties, including adsorption, mobility, colloidal stability, surface charge, surface roughness, porosity, and hydrophobicity [15, 16].

Micro and nano plastics (MNPs) have the potential to translocate into the biological tissue and accumulate [17, 18]. These interactions can lead to toxicity, including, decreased reproduction, hypoactivity, and other defects [17, 18]. Polystyrene is a commonly used plastic [15]. It has many applications including the manufacture of various packaging materials [19]. It has several reasons, such as its good plasticity, easy manufacturing, and low price [19]. As mentioned, it is one of the most prevalent plastics in the marine ecosystem and can harm fish in many ways, such as immune responses in Fathead minnows and lesions in the Zebrafish's liver, as well as the behavior, physiology, and metabolism of Crucian carp [12, 20]. Therefore, any fish in the marine ecosystem may be affected by NPs through direct ingestion, their gills, or indirectly through the food chain [20].

In order to achieve a better understanding of the fates of plastic debris in the environment and their impacts on organisms and microorganisms, many studies have been focused on this issue. Some studies mainly focused on the production of plastics, their characterizations, and their behaviors and changes (i.e., aging) in different environments [15, 21-25]. In addition, many studies have investigated the toxicology of plastics and their adverse effects on biological systems [17, 18, 26, 27]. However, the majority of these works study the spherical MNs, which is not realistic in nature. Moreover, no studies made the regularly shaped and irregularly shaped plastic particles and compared them with their aged ones. Therefore, this study tried to develop a procedure for engineering plastic particles to closely resemble the debris plastic in nature. It provides better insight into the changes of the plastic in the environment. In addition, their

applicability in environmental testing, e.g. toxicology, assists the investigation of the plastics' fate and their impacts on live systems.

Chapter 2: Background, and Literature Review

2.1 Introduction

The term plastic refers to materials formed from modified polymers using additives to meet industrial processing technologies' demands [28, 29]. Plastics are organic materials whose outstanding formability and mouldability make them applicable to a wide range of applications [30]. Based on their intermolecular bonding, they can be categorized as thermoplastics and thermosets [30]. Thermoplastics soften when exposed to moderate heat, appearing as rubber-like liquids. When cooled, they return to a glassy or semi-crystalline solid [30]. High-production volume thermoplastics include ABS (Acrylonitrile, Butadiene, and Styrene), acetals, acrylics, cellulosic, fluorocarbons, polyimides, polycarbonates, polyethylene, polypropylenes, vinyls, and polystyrenes [30]. Thermosets differ from thermoplastics. Thermosets are not meltable, when they are exposed to heat, they will undergo chemical decomposition and irreversible changes in their structure [31]. As a result, they are not recyclable after production [32]. Thermosets are generally more robust and nonflexible polymers, leading to different applications than thermoplastics in the plastics industries [30, 32]. The thermosets are alkyds, allylics, amines, epoxies, phenolics, polyester, silicones, and urethanes [30].

Polystyrene is a common thermoplastic used in a wide range of applications, including packaging (e.g., food products), medical supplies, construction (e.g., insulation materials), and the automotive industry (e.g., door panels and instrument panels). The molecular weight (*MW*) of styrene (the PS monomer) is 104.15 g/mol, but the *MW* of the polymer depends on its structure (i.e., the number of monomers that produce it), often falling in the range of 3,600 – 2,900,000 g/mol [33]. Polystyrene is reasonably thermally stable; significant bulk degradation is not observed at temperatures lower than 200 °C [34]. Its glass transition temperature (the temperature

at which the polymer changes from a glassy state to a rubbery state, T_g) is 95 – 100 ℃ [4, 35]. It is different from the melting point, which is the temperature at which the state of crystalline polymer changes to the viscous flow [36]. In the case of PS with 35,000 g/mol molecular weight, the common experimental melting point of PS is 240 ℃. Above 330 °C, PS rapidly degrades to its monomers [34]. The density of plastic particles plays a significant role in determining fate in aquatic environments. Plastic particles such as PS and PVC with a greater density than water (i.e., the density of water between 0 – 40 ℃ and a pressure of 1 atm is almost 0.99 g/cm^3) sink in the water, while they float if their density is less than water (e.g., PE and PP) [14, 25, 37]. The density of PS is generally in the range of 1.01-1.3 g/cm^{3,} depending on different parameters, including temperature. For instance, the density of PS is 1.05 g/cm^3 at 20 ℃ [38]. As such, PS tends to float or settle slowly in water, allowing it to stay suspended for significant periods in, e.g., rivers and lakes. Macroplastics' buoyancy/sedimentation properties mainly relate to their density [14]. While density does not change with size, the balance of forces on the particle's changes at smaller sizes. When plastic particles break down into smaller sizes, including micro-scale or nano-scale, due to aging, they may be more stable in the water column [14, 25]. While PS is insoluble in water, it can be dissolved in many organic compounds (e.g., chloroform, acetone, tetrahydrofuran, toluene, and benzene) [39].

2.2 Micro and Nanoplastics

Plastics in the environment exist across a wide range of sizes, which are often categorized into mesoplastics (5 – 25 mm), MPs (0.1 – 5 mm), and NPs (<10^{-4} mm or <10^{-3} mm) [4, 23, 28]. The upper size limit of NPs is not currently universally agreed upon. Reports have considered either 100 nm or 1,000 nm cut-offs for nanoplastics due to the field of study or applicability. Generally, nanoplastics show properties that are not exhibited by larger plastic particles [28, 40].

The uncertainty of NPs' definition is also visible in regulations [41]. Different organizations have their own definition of nanoplastics, making it difficult to have uniform rules [28, 41]. For instance, in 2011, the European Commission (EC) defined nanoplastics as plastic particles where 50% or more of the population has a size distribution of 1-100 nm [41]. Based on this definition, nanoplastics are counted as nanomaterials [41]. In the USA, plastics regulations vary from agency to agency, including the US Environmental Protection Agency (USEPA), The US Food and Drug Administration (FDA), the US Department of Agriculture, The Occupational Safety and Health Administration (OSHA), and the Consumer Product Safety Commission (CPSC), based on the various purposes [42]. According to the International System of Units, there are some agreements for the size of macroplastics (plastic pieces larger than 1 mm) and microplastics (plastic pieces between 1 mm and 1 μm), so the size of nanoplastics would range from 1nm to 1000 nm/1 μm. Considering these classifications, regulating the upper size limit of nanoplastics to 100 nm appears to not be due to scientific reasons [42]. Apart from the set upper size limit for the NPs definition, if they have the properties of nanoparticles, they count as nanoparticles [40].

In general, there are several differences between MPs and NPs. Brownian motion is the dominant phenomenon compared with buoyancy and sedimentation for NPs in suspensions compared with MPs. In addition, the NPs' surface possesses many molecules, leading to more surface area-related chemical reactions than physical ones. Also, the NPs' size causes higher bio-absorption, translocation, and transport through biological membranes [40].

Due to their size, they have a high specific surface area (i.e., the total surface area of the plastic particles per unit of its mass/surface-to-volume ratio) and different physical characterizations compared to bulk materials, including lower melting points and density [40]. Moreover, the nanometer dimensions of nanoparticles influence their behavior dramatically, such

as characteristics related to the particles' surface, movement and the fate of particles, and interactions of particles with organisms [24, 40, 43]. Therefore, understanding the size, surface charge, shape, and surface areas as fundamental features are essential steps to predicting nanoplastics' behavior and fate [24].

For instance, one key behavior of nanoparticles is that they do not immediately settle at the same rate as larger particles, which impacts their fate in aquatic systems. Reducing the size of plastic particles leads to an increase in the relative impact of particle diffusion and shear stresses (both of which contribute to particles remaining in the water column) and a subsequent decrease in the relative impact of gravity, leading to diminished sedimentation [40].

$$V = \frac{2r^2(\rho_{sphere} - \rho_{fluid})g}{9\mu} \qquad \text{Eq. 1}$$

Stokes' law (Eq. 1) describes the falling rate of spherical particles in fluids [44], where V is the sphere velocity in a fluid, r is the radius of the sphere, ρ_{sphere} and ρ_{fluid} are the density of the sphere, and fluid, respectively, g is the gravitational acceleration, and μ is the fluid viscosity [45].

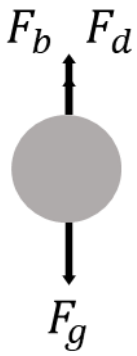

Fig. 1 – Schematic illustration of forces affecting a particle in the aquatic media.

As illustrated in Fig. 1, a spherical particle in a quiescent fluid exists under three forces, namely buoyancy force (F_b), drag force (F_d), which act upward on the sphere, and gravitational attraction ($F_g = m \times g$), which acts downward [45]. A particle's terminal settling velocity, the stable rate at which a particle would fall in a column of infinite length, is obtained when the sum of the upward forces, F_b and F_d equals gravity, F_g. [45].

At smaller length scales, the inherent kinetic energy of nanoparticles in aquatic environmental systems will cause collisions with water molecules and other matter, leading to random movement or Brownian motion, although it takes much longer time for particles to move longer distances by this phenomenon [25]. As particle size decreases, however, Brownian motion becomes the dominant component of transport in media, which will hinder sedimentation. For this reason, NPs which have not aggregated are inclined to remain in suspension [14, 25]. In this scenario, collisions, and water dynamics (e.g., flow and waves) are two essential parameters that cause plastic particles to travel remotely in open waters [14, 25, 46]. Although the colloidal behavior of NPs leads to their slower vertical movement in water columns compared to MPs, the interaction of NPs with natural colloids, microorganisms, or other ions can influence their sedimentation velocity. For example, aggregation can increase the effective size and lead to

enhanced settling [28]. However, for particles in the nano-size fractions, settling velocity decreases to the point that they are metastable and can travel significant distances.

Along with the size of a particle, the surface charge of particles can affect the fate of nanoparticles causing aggregation of plastic particles or absorption into microorganisms [24, 40]. The aggregation of MPs and NPs will dramatically affect their properties, including stability, toxicity, bioavailability, transportation in fluids, and fate [46, 47]. The surface charge has an essential role; according to DLVO theory, the electrical double layer structure is formed by the charge on the surface of the particles because of adsorption, hydrolysis, ionization, etc. [47, 48]. This theory describes the stability or lack of stability of charged particles that are close to each other due to the combination of van der Waals attractive and electrostatic repulsive forces. These forces oppose each other, and greater electrostatic forces produce energy barriers to aggregate formation [47, 48].

While DLVO theory is applicable to nanoparticles, it is often observed that aggregation does not comply with this theory [47]. Hence, extended DLVO theory has been developed to consider forces, including hydrodynamic attractions and ion-specific effects, not taken into consideration in DLVO theory [49].

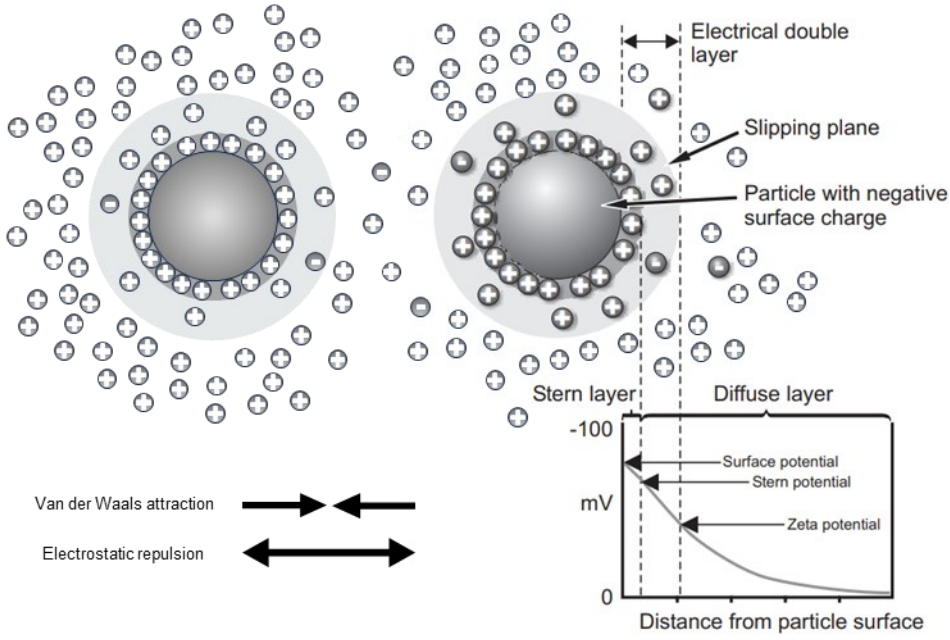

Fig. 2 – Schematic illustration the combination of a negatively charged NP's double layer and DLVO theory (adopted from Zetasizer manual [50]).

Fig. 2 illustrates the electrical double layer structure, which is composed of the ions in solution surrounding a charged nanoparticle (e.g., negatively charged nanoplastics). The layer consists of two parts: the Stern layer and the slipping plane within the diffuse layer. The surface of a negatively charged particle attracts cations. As shown, the Stern layer is the closest layer to the particle's surface made by a high concentration of the cations adsorbed to the surface of the anion (i.e., only the cations located tightly on the main anion's surface). The layer of surrounding liquid includes a lower concentration of cations accompanied by a few anions diffused from the bulk. The outer boundary of this layer is called the slipping plane. Zeta potential is calculated from electrophoretic mobility and indicates the charge at this point in the suspension. Slipping plane attaches to the bulk from the outer side. The diffuse layer consists of slipping plane and the bulk, which includes free ions plus a high volume of the counterions. Any surrounding charged particles in bulk (i.e., the outer side of slipping plane) behave as a single object [51, 52].

In general, the solid and liquid parts of the suspension have various energy levels. When they get into close contact, tension occurs at their interface. For example, as solid particles are dispersed in the water, they carry a negative charge due to duo to the high dielectric constant of water. So, the cations in the media attract the particles with negative charges, leading to a fixed immobile layer (stern layer) surrounding the negatively charged particle's surface and partially neutralizing it. The residue of anionic charge attracts more cations, forming the second layer further away from the particle's surface (diffuse layer). This layer is mobile and less concentrated since the anionic charges weaken because of the distance. The line between the two mentioned layers is a shear plane and its potential is called stern potential. Displacing of the diffused ions from the surrounded particle creates a measurable potential difference (ZP).

The aggregation process consists of physical transport (diffusion) followed by attachment (binding) [47, 53]. Considering quiescent conditions, transport is achieved through diffusion [47, 54, 55]. Brownian motion, hydraulic shear, and gravity sedimentation are the main factors for diffusion which brings particles close to each other, causing collisions [47, 54]. When a particle collides with another particle, that provides the opportunity for attachment. If the energy barrier is not prohibitive, they may bond due to attractive forces such as van der Walls forces, electrostatic interaction, and chemical bonds. In this step, aggregates are formed [47, 54]. The rate of agglomeration/aggregation depends on the number of collisions combined with the propensity of attachment during each collision [54]. Nanoparticles are often more stable in aquatic environments than microparticles [47]. Brownian motion is the dominant factor in particle transport in the nanoscale, while at larger sizes, settling becomes more pronounced [47, 56].

2.3 Production of Microplastics and Nanoplastics

Generally, MNPs are produced through either a top-down or bottom-up approach [21, 57-61]. The top-down approach prepares nanoparticles by decreasing the size of larger particles by breaking them down into smaller fragments [57, 60, 61]. This route may use techniques such as wet and jet milling, high-pressure homogenization, and stator homogenization [57, 60, 61]. Top-down approaches have several significant disadvantages that restrict their application; the costs are relatively high, compared with bottom-up techniques, since they require expensive equipment and conditions such as high-pressure pumps, specially designed nozzles, and high pressures and temperatures [57, 60, 61]. They are also often time-consuming, have poor control, and result in particles with a wide size distribution.

In contrast, bottom-up approaches typically begin with dissolved precursors that are induced to change phase, leading to nucleation and particle growth [60]. This category employs different methods such as supercritical fluid technology, spray freezing into liquid, evaporative precipitation into an aqueous solution (EPAS), and liquid anti-solvent precipitation (LAS) [57, 60, 61]. These approaches are generally employed at ambient temperatures and pressures and need relatively simple equipment [57, 60, 61].

Of the mentioned techniques, LAS can be considered a simple method, consisting of three primary steps: supersaturation, nucleation, and subsequent particle growth [57, 61]. This procedure is based on differing solubilities of a compound in different liquids, i.e., soluble in one liquid and insoluble in another [57, 61]. The nucleation step is described by classical nucleation theory, where the formation of crystals as a new phase (e.g., solid phase) is due to the assembly of some molecules in the metastable old phase (e.g., liquid) [57, 62, 63]. A requisite for this step is the supersaturation of a solution [57, 61]. Supersaturation is achieved by dissolving the

compound of interest in a solvent, which is then added to a larger volume of an anti-solvent. Subsequently, the compound, now supersaturated in the anti-solvent, undergoes nucleation as precipitates begin to reduce the concentration of the dissolved compound [57, 61]. Following nucleation, particle growth occurs due to condensation and coagulation [60].

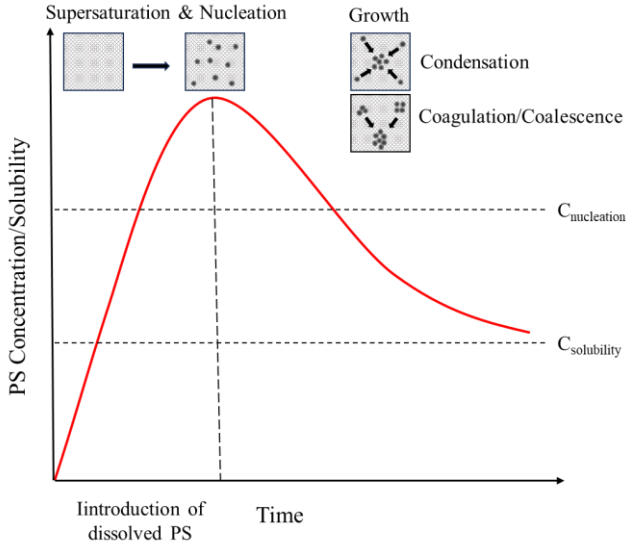

Fig. 3 – Schematic illustration of the steps of the LAS technique (supersaturation, nucleation, and growth), showing the formation of PS particles (adapted from [39]).

Fig. 3 illustrates the three steps of LAS based on the plastic particles' surface energy changes for PS. As illustrated, the concentration of PS as a solute rises as it is introduced until it reaches the supersaturation condition, and at a specific concentration of PS (the minimum concentration for the suspension, ($C_{nucleation}$), initial nucleation is started which is more than the equilibrium concentration ($C_{solubility}$) or above the solubility value [61]. Nucleation causes a decrease in the

concentration of the solute and the start of the growth phase at $C_{nucleation}$ simultaneously. This phase will stop when the solute's concentration reaches $C_{solubility}$ or solubility [61].

These steps can be explained by the Ostwald ripening phenomenon, which discusses saturated systems' coarsening and recrystallization procedures [62, 64, 65]. According to this phenomenon, the small particles in a dispersed environment possess a higher surface energy than bigger particles, which is a prerequisite for nucleation. Then in the growth step, the formed nuclei grow quickly by consuming the old phase, i.e., they grow via interaction with solute, leading to a high solute concentration on their surface [62]. Agglomeration occurs simultaneously with the growth of the species [57, 60]. The growth is ended when the mass of the new phase meets almost the equilibrium mass [62]. In other words, the growth species' concentration reaches equilibrium [57, 61]. After this step, coarsening, also known as the Ostwalt ripening phenomenon, is started, in which the precipitation phase happens due to shrinking the surface free energy [62].

Several parameters affect the particle size and the particle size distribution in this method. These include the volume ratio between solvent and anti-solvent, solvent introduction flow rate, stirring rate, polymer, pH, the concentration of the compound, the technique of precipitation (e.g., supercritical anti-solvent precipitation, liquid anti-solvent precipitation, spay drying), solvents, and temperature [21, 57-61].

There are two different pathways for anti-solvent precipitation regarding the usage of surfactants [22]. Surfactant helps stabilization of particle size in a suspension [22]. Surfactants such as amphiphilic molecules are formed in the polar hydrophilic heads and the nonpolar hydrophobic tails [66]. Examples of commonly used surfactants are polyvinyl alcohol (PVA), sodium dodecyl sulfate (SDS), and Tween 20 [52, 67]. The structure of surfactants capacitates

them to construct three-dimensional structures by self-assembling [66]. The role of surfactant molecules is to decrease the surface tension of a water-based/aquatic matrix to stabilize and disperse particles, including nanoparticles [68, 69].

Anti-solvent precipitation has many industrial and commercial applications, including drug and pharmaceuticals [57, 60, 61, 70, 71], agriculture [72], rubber [73], and the preparation of MNPs [21, 74, 75]. Many scientific studies have been run based on this technique in the drug and pharmaceutical industry to increase the solubility and bioavailability of poorly soluble drugs via methods such as the production of nanoencapsulation and nanosizing drugs [76, 77].

For example, Wu and Wang (2022) applied it to prepare nanoparticles of several drugs, i.e., curcumin (CUR), coumarin 6 (COU), nortriptyline hydrochloride (NOR), amitriptyline (AMI), prochlorperazine dimeleate (PRO). In this procedure, drug solution was added to the anti-solvent individually employing the 1 or 2 mL/min injection rate under a 1000 rpm stirring rate. Results showed that the flow rates had a minor effect on the average particle size, but the increase caused a narrower size distribution. The resulting particle size ranged from 152 to 745 nm and depended on the drug type [57]. In another work, curcumin nanoparticles were fabricated with two precipitation techniques under the same mixing rate, obtaining particles ranging from 330 to 850 nm [61].

In addition, there are several studies using LAS to make nanoplastics [21, 74, 75]. Takana et al. (2021; 2023) produced nanoplastics from various polymers, such as PS and low-density polyethylene (LDPE). For instance, the former study prepared PS nanoscale particles, 226 nm, by dissolving PS in their toluene with heat assistance and was injected into an anti-solvent (water/ethanol) to precipitate under the stirring rate of 1000 rpm. In the latter paper, the

nanoparticles of a polymer (low-density polyethylene, LDPE), 432 nm, were made with a similar methodology. The nanoparticles have a large particle size distribution (approximately 400 – 1000 nm). In both studies, particles were spherical [21, 74]. Also, Zhao et al. (2020) produced PS nanoparticles by rapidly adding the prepared PS in tetrahydrofuran (THF) solution to water with no surfactant as an anti-solvent, 1:9 ratio, and mixing with a 1000 rpm stirring rate to make the spherical nanoparticles with the size range of 50 – 200 nm [22].

In another study, the polyvinylpyrrolidone particles (PVP) were prepared with a supercritical anti-solvent precipitation technique by a mixture of solvents and a supercritical anti-solvent to decrease the particle size from 0.11 μm to 3.80 μm [75]. For instance, pure EtOH provided 2.42 μm mean diameter microspheres, while the mixture of acetone (AC) and EtOH as the mixture solvent with the composition mass percentage of 70/30 decreased the particle size to 0.22 μm [75].

2.4 Primary and Secondary Plastics in the Environment

Plastic pollution has two main sources: primary and secondary [25, 78]. The primary sources of plastics are industrial plastics of different sizes manufactured deliberately, as discussed above [25, 78]. Secondary sources or secondary MPs and NPs are derived from the aging procedures of primary (macro)plastics (e.g., commercial plastic) and breaking them down into smaller particles [25, 78]. When plastics are introduced to the environment, they start aging due to environmental inducements [4, 79]. This process lasts hundreds of years, but plastic particles undergo different aging factors such as UV light oxidation, temperature changes, and mechanical abrasion, after which their size reduction is accelerated [28]. These factors cause weathering due to various chemical changes such as hydrolysis, photooxidation, chemical oxidation, and biological degradation [1, 6, 80]. Photooxidation and photothermal degradation, which occur through a

combination of solar radiation (i.e., UV light and heat) and oxygen, have significant roles in degradation [1, 79]. UV light with the wavelength domain 100 – 400 nm falls between infrared light (λ = 1 – 700 nm) and visible light (λ = 400 – 700 nm) [1]. Based on the wavelength, it is categorized into three regions: UVA (λ = 320 – 400 nm), UVB (λ = 280 – 320 nm), and UVC (λ = 100 – 280 nm) [81]. It is noteworthy to mention that UVC light completely and UVB light mostly are absorbed by the ozone layer in the atmosphere [1]. The received UV light on the earth weakens the surface of the plastic particles through the reduction of elasticity by oxidation of the polymer chain and makes the particles fragile [1, 79]. Then, the brittle plastic fragments are more susceptible to mechanical shearing by other objects, such as other plastic wastes or sand and rocks, and friction with water due to wind and waves [79, 82].

UV photooxidation contains three steps: initiation, propagation, and termination [1]. The process starts with the absorption of photons by chemical bonds of polymer chains which leads to breakage in them and the production of free radicals [1]. The breakage occurs for weak C-H bonds in tertiary carbons. Then, the present oxygen reacts with the produced free radicals to make proxy radicals [1]. The new free radicals retreat hydrogens of vicinal chains and produce new free radicals and hydroperoxide groups [1]. This chain reaction ends with a combination of all free radicals and the formation of stable groups [1].

Some studies collected plastic debris (weathered plastics) in the environment (e.g., aquatic environment) and characterized them and in some cases compared them with their nonweathered counterparts. In general, particles that have been weathered by nature are smaller, irregularly shaped, and oxidized [83-85].

For instance, PE plastic debris (coffee packing items, W-PE) was collected from the North Atlantic subtropical gyre and some of their features were compared with their nonweathered

original items (N-PE) [84]. The number-average molecular weight (M_n) and *MW* of the W-PE sample were lower (7.1 kg/mol and 67.5 kg/mol, respectively) compared to N-PE (12.3 kg/mol and 94.0 kg/mol, respectively). This suggested the aging resulted in breaking the polymer chain, decreasing the molecular weight. Micro-Fourier transform infrared (μ-FTIR) mapping, i.e., a technique using a combination of the principles of Fourier Transform Infrared (FTIR) spectroscopy with spatial mapping abilities at a microscopic scale, was used to study carbonyl index (i.e., a quantitative parameter indicating the relative presence of the carbonyl functional group (-C=O) in the sample of the cross sections of the sample [8]. The carbonyl index for N-PE was small and uniform across the surface of the particles. However, W-PE had a highly oxidized surface, resulting in a larger carbonyl index. Additionally, W-PE oxidation was more intense towards the particle center. The results of infrared spectroscopy coupled to atomic force microscopy (nano-AFMIR) of W-PE detected ketones, carboxylic acids, and lactones on the surface. SEM images of W-PE indicated a rough surface and deep cracks. In a related study, PE microplastics also collected from the North Atlantic subtropical gyre were very fragile particles due to chipped surfaces with many cracks[85]. In addition, some nano particles were detected on their surface as well. FTIR of the samples indicated the presence of a broad carbonyl group bond.

Polystyrene MPs debris was investigated on the Tuul River shore in Ulaanbaatar, Mongolia [86]. Polystyrene foam (PSF) was the dominant MP in that region, which was attributed to the high consumption of heat insulators. The initially white color of PSF changed to a brownish hue in the environment because of the aging process. Additionally, the plastic foam pieces broke down into smaller fragments. An elevated carbonyl index was observed on the surface of the collected samples. The MPs were observed to be less than 1 mm, which was smaller than the size of PSF particles collected from shore which had undergone less degradation.

Expanded PS (EPS) microplastics were collected from the Pearl River Estuary in South China beaches for one month [87]. The EPS samples ranged from 0.03 mm to 5 mm and MPs with the size 1 – 2 mm were the most abundant MPs. The surface texture of the EPS MPs was rough with folds, cracks, and irregularly shaped pores, while the surface of the new EPS plastics was smooth and flat with the regularly shaped mesh structure. These changes are likely due to oxidation by the combination of mechanical abrasion and photooxidation.

A few studies have focused on the types of MPs debris and their distribution in the environments [83, 88, 89]. For example, microplastics in the sediment and agglomerated sewage water (Bahir Dar, Ethiopia) were studied [83]. Several different types of plastics were identified using FTIR, including PP, PE, PVC, PA, PET, & PS. The morphologies of microplastics widely varied, including fragments, fibers, films, pellets, and foams. Their particle size ranged from 0.00417 to 0.5 mm.

To investigate the natural weathering process, Shi et al. aged PS samples (50 mm × 80 mm × 3 mm) for a year in selected coastal waters ranging from China to Europe [90]. Following exposure, the PS samples were oxidized. Carbonyl and hydroxyl groups appeared in FTIR analysis at 1500 – 1800 cm^{-1} (1713, 1720, 1735, and 1780 cm^{-1}) and 3000 – 3800 cm^{-1}, respectively. Observation of the samples' morphology after exposure indicated rough surfaces with many cracks and chipped smaller particles compared to the bright, clean, and smooth surface of samples before exposure. Their color turned yellow during the exposure and darkened throughout the exposure period.

Many other works have been assigned to study the weathering procedure of plastic particles in marine environments [8, 25, 82]. Plastic particles in the aquatic environment are a mixture of various polymers, including PE, PP, PVC, PA, PET, and PS [25]. One of the most commonly used

plastics, and more often detected in the environment, is PS [16, 73, 91, 92]. Hence, it makes it one of the critical plastics choices to study individually or with other plastics [16, 82].

The impacts of UV radiation and high temperature were examined separately on the degradation of several MPs, i.e., PP, HDPE, LDPE, and PS [8]. All plastics exposed to UV light and high temperature were weathered, although the intensity of aging by each factor was different on each plastic. For instance, PS was oxidized more with the higher temperature compared with UV radiation. In general, the exposure of MPs produced nano-size particles (<1000 nm), although still some particles with micro-size present. Also, characterization by SEM illustrated the irregular shape of produced NPs.

The mechanical fraction of plastic particles is another aging factor [82, 93, 94]. Ekvall et al. (2019) prepared PS nanoplastics from expanded PS foam and PS coffee cup lids mixed with milli-Q water (MQW) by mechanical sheering using a household immersion blender; the process followed with filtration (0.45 μm and 1.2 μm filtration for foam and 0.8 μm filtration for the particles from coffee cup lids). The particles had many different shapes. Their surface charge was negative or close to neutral. The particle size of the foam was 167 ± 4 μm with a polydispersity of % PD 24. The particle size of the particles from coffee cup lids was not appropriately reported, but it mentioned that they included some particles with smaller sizes than foam [82].

In another study, PS and PE nanoplastics, called nano-PS and nano-PE, respectively, were made by a blade grinder and a planetary ball mill. Then they characterized them to find out their features, such as morphology, mean size, and surface charge. For example, the particle size of nano-PS by this method was 306 ± 15 nm, and its ZP (ζ) was – 44 mV. It is noteworthy that the size of the milling balls had some impact on the amount of aggregation/agglomeration of the plastic particles [93].

2.5 Toxicity

As mentioned, plastics are degraded in the environment and fragmented into smaller pieces (i.e., one MP can produce billions of NPs). The particle size of MNPs, especially NPs, plays a vital role in their interactions with biological systems (e.g., plants, bacteria, vertebrates, amphibians, reptiles, and mammals [17, 18, 26, 95]. Their small size provides various pathways, such as ingesting and inhaling, for them to penetrate different organisms by passing through the biological barriers, for instance, cell membranes, mucous layers, and tissues [17, 26, 27, 95]. They can be penetrated into organisms directly through feeding and indirectly by respiratory pathways and adsorption to the skin. In addition, it can transfer via the food chain [17, 96]. The penetration occurs through interaction with biomolecules [17, 97]. MNPs can accumulate in different organs such as gills, liver, and gut after translocation in the living systems [17, 18]. This has brought up another concern related to MNPs particles, which is their potential toxicity due to their large surface area since there is evidence demonstrating they as a vector of organic and inorganic pollutants [17, 18, 27]. For instance, NPs may behave as Trojan horse to transfer the pollutant molecules [17]. After entrance to biotas, they can accumulate in tissues and cause different biological problems, including increasing oxidative stress, changing enzymatic and genetic performance, and cancer [17, 18].

There are many studies focusing on the adverse impacts of MNPs on organisms and in particular bacteria [26, 95]. NPs probably can impact the soil microorganisms' physiology either by attaching or penetrating microbial cells [95]. The known adverse impacts of NPs on bacteria include deduction in growth activity, enzyme activity, cell surface charge, and changing patterns of biofilm formation [26]. For example, binding PS NPs to bacteria cell surfaces can restrain growth and can cause oxidative stress [98]. Another investigation revealed that the exposure of

some types of aerobic bacteria to PS NPs led to an increase in oxidative stress and the reduction of the cell's life [99].

Chapter 3: Material and Methods

3.1 Preparation of Primary Polystyrene

3.1.1 Dissolution and Anti-Solvent Precipitation of Polystyrene

Spherical PS particles were prepared via anti-solvent precipitation. Pristine PS (*Sigma-Aldrich*, Average MW ~ 192,000) pellets (240 mg) were dissolved in 12 mL chloroform (*Fisher Scientific,* HPLC grade) with magnetic stirring at room temperature (19 ºC) to prepare a 20 mg/mL solution. The anti-solvent was prepared as 10% PVA, which was selected among 0.1%, 1% and 10% PVA solution (*Millipore Sigma*, 87-89% hydrolyzed, MW 13,000 – 23,000) dissolved in MQW. Dissolved PS was introduced into the anti-solvent using a syringe pump (*NE-1000 Series of Programmable Syringe Pumps*) loaded with a 30 mL glass syringe (*Millipore Sigma*) and 12 G Teflon needle (*Sigma Aldrich*, *PTFE syringe tubing, 12 in length*), resulting in a final volume concentration ratio of 1:30. The final employed pump rate and needle size were selected among different tested pump rates (0.1, 0.25, 0.5, and 2.6 mL/min) and sizes of Teflon needle (12, 18, and 23 G). The suspension was then stirred for 3 h in a fume hood.

3.1.2 Reduction of PVA concentration

Following particle formation, PVA was removed from the suspension by six times batch-wise centrifugation (*Thermo scientific*, *Sorvall Lynx 4000*) at 14,000 × *g* at room temperature. The first centrifugation step was set to 40 min to account for the greater viscosity of the suspension containing 10% PVA, while each subsequent step was performed for 20 minutes. Centrifugation separated PS particles from the solution, and the supernatant was subsequently removed and replaced with MQW. Samples were resuspended and combined after each wash step, resulting in

the concentration of PS in suspension and removal of PVA. Following the 6th centrifugation step, the resulting supernatant was collected to determine PVA concentration with a Total Organic Carbon (TOC) analyzer (*Shimadzu TOC-L CPH analyzer*). Suspensions were considered washed of PVA when TOC measurements were less than the detection limit of ~ 2.00 mg C/L.

3.1.3 Measurement of the Concentration of the Washed Plastic

The concentrations of these washed samples were calculated from the mass of a deposited sample using a microbalance (*Sartorius Corporation, MC 5*, Min = 0.001 mg). The mass of each aluminum weigh boat was found, after which known volumes of suspension (50 – 150 μL, depending on anticipated concentration) were added. Weigh boats were then desiccated until they were dried completely (1 – 3 days). Samples were considered dry when a reference weigh boat loaded with an identical volume (50 μL) of water measured zero change in mass compared to the weigh boat before MQW addition. Finally, a balance check was performed using a weigh boat to which neither sample nor MQW was added. Any observed change in mass was attributed to the balance, and measurements of plastics deposition were normalized accordingly.

3.2 Preparation of Secondary Polystyrene

3.2.1 Preparation of Ground Plastic Particles from Polystyrene Pellets

Irregularly shaped PS particles were produced in four steps: coarse grinding PS pellets into a powder, ball mill grinding the powder into weathered particles, filtration for size selection, and concentration of the resulting particle suspension. For each sample of secondary PS, ten 5 g batches of PS pellets were ground into a powder using a household coffee grinder (*MASTER CHEF* Coffee Grinder/Herb Mill Grinder, 12-cup) for 10 min in total in 30-second pulses with 5-second pauses in between. Following each batch, the grinder was allowed to sit and cool for 5

min. Then, each batch of the resulting powder was mixed with 2 to 3 mL ethanol (anhydrous ethyl alcohol, *Greenfield Global Inc., P016EAAN*) and transferred into a zirconia vial containing one zirconia ball. The paste was milled continually for 10 min by a ball mill grinder (*SPEX Sample Prep, Mixer/Mill 8000*). Then, the ground paste was collected and stored in 50 mL glass vials for filtration.

3.3 Size Selection and Condensation

3.3.1 Microparticles of Primary and Secondary plastics

Both primary and secondary plastics production methods resulted in suspensions with a wide distribution of particle sizes. Therefore, the size separation was performed through several filtration steps. The washed primary plastic samples obtained as described in section 3.1.2 were diluted to ~ 0.45 mg/mL to avoid clogging the filters. These diluted samples were then filtered through a 10 μm polyflon filter (*Advantec*) to remove the largest particles. The filtrate was collected as a primary sample with a particle size of less than 10 μm.

Secondary plastics were pretreated through a sedimentation step. The process of isolating small particles from bulk was initiated through the addition of ~ 2 mL ethanol to each ground batch following ball mill grinding. Then, the heterogeneous suspension was shaken and let to rest until the separation between the cloudy supernatant and settled particles appeared. The time needed for the larger particles to settle out from the cloudy supernatant differed for each batch and was determined visually. Then, the cloudy supernatant was collected and added to a 100 mL glass beaker filled with 40 mL MQW. This procedure was repeated six times for each batch, after which the collected mixture of MQW and small particles was filtered with the 10 μm polyflon filter. The process was repeated for all 10 batches, and their collected mixtures were combined to make one secondary PS sample with a total volume between 600 mL to 800 mL.

For both cases, the collected filtrate following 10 µm filtration was then passed through a 5 µm mixed cellulose ester filter (*Millipore Sigma*) under a vacuum along with an overhead stirrer system (*Joanlab*) at a mixing rate of 500 rpm. 150 mL of the prepared sample was added to the glass Büchner funnel. The solvent level in the funnel was not allowed to drop below 100mL, providing enough volume for stirring. When the complete sample had been added, the inside of the funnel was washed with 50 mL MQW, and the filtration continued to the point that 20 mL of the sample remained in the funnel. This remaining supernatant above the 5 µm filter was collected as microplastic suspension samples. These dilution and filtration steps resulted in diluted PS microplastic suspensions with a targeted particle size between 5 µm and 10 µm, which were concentrated via rotary evaporation (*Büchi, Rotavapor R-200*), which simultaneously washed the residue of ethanol in secondary samples as well. Sample concentrations were then identified following the method described in section 3.1.3.

3.3.2 Nanoparticles of primary plastics

The separation of the primary NPs from the bulk was initiated by resting the suspension sample with no disturbance for 17 days in a fridge. After the required period, the supernatant was collected and diluted 1:10 in MQW. The diluted suspension was filtered with a 10 µm filter. The filtrate was then passed through the 5 µm filter under a vacuum using the same method detailed in section 3.3.1, and the filtrate was collected as a nanoplastics sample and concentrated using a rotary evaporator. The final concentrations were ~ 0.16 mg/mL.

3.3.3 Nanoparticles of secondary plastics

The filtrate (smaller than 5 µm) collected in the preparation process of the secondary microplastic sample (section 3.3.1) was filtered with 1.2 µm filters (*Millipore Corporation*) and 0.8 µm nitrocellulose membrane (*Cole-Parmar*), respectively, with the same procedure mentioned

in section 3.3.1. The filtrate was collected as PS secondary nanoplastics with a particle size of less than 0.8 µm. Then, it was concentrated using the rotary evaporator. The final concentrations were ~ 0.20 mg/mL. Fig. 4 shows the production flowchart of primary and secondary MPs and NPs.

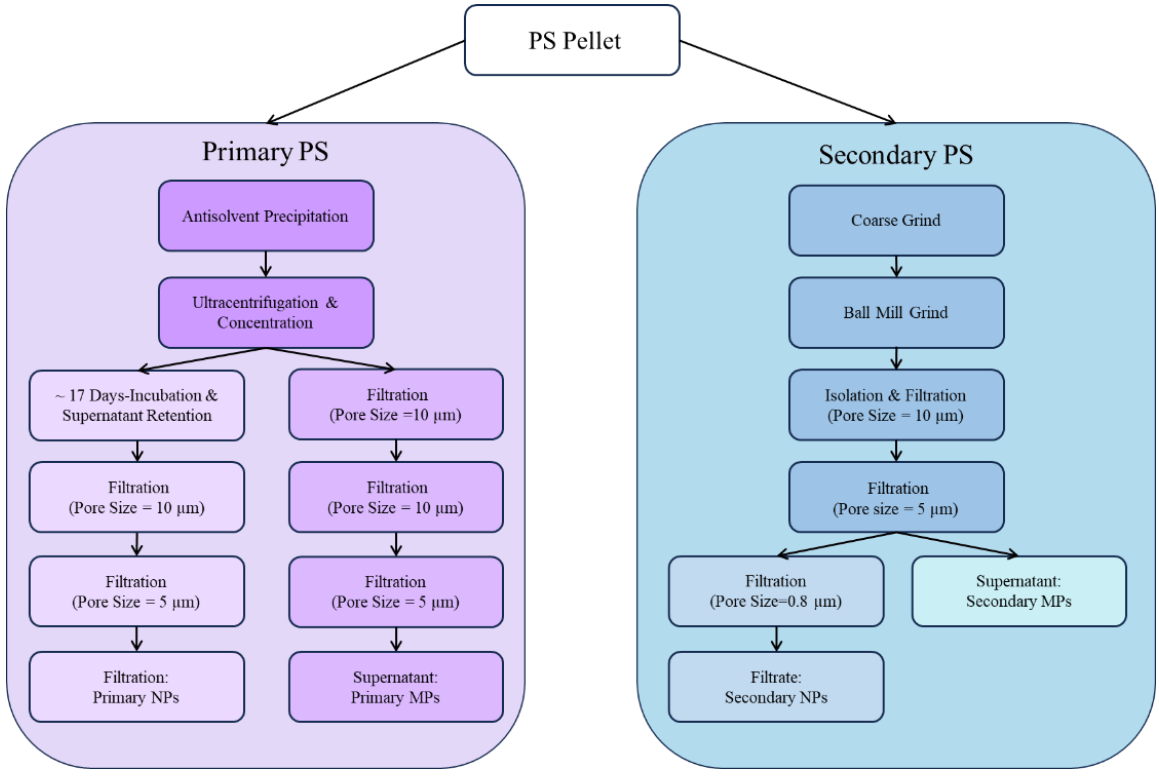

Fig. 4 – Flowchart of the production steps of the primary and secondary MPs and NPs

3.4 Preparation of UV Light Exposed (Weathered) Primary and Secondary Polystyrene Micro and Nanoplastics

Weathered samples were produced through UV exposure of the heterogeneous primary and secondary NPs suspensions.-The UV light setup consisted of a chamber with white walls with a UV – Vis light lamp (*XM lighting, Mogul*, 250W, 10,000K). Plastic suspensions were placed in 8 mL clear glass vials located at specific spots on a vial roller (*Fisher Scientific, globe SCIENTIFIC*

INC.) that were located beneath the UV lamp. The roller was placed at such a distance from the lamp that it was adequately close to the UV lamp to receive a high radiation intensity (average intensity of 1,352 ± 127 $\mu W/cm^2$) while ensuring the plastics' melting point was not met. The vial roller continuously rotated (~ 40 rpm), exposing the prepared samples to UV light for five days.

The specific placement of vials was determined by mapping the UV intensity to determine locations with uniformly high radiation intensities. Average radiation intensity was measured at ten spots in each of the five rows of the vial roller using a radiometer (*Fisher Scientific, UVX Radiometer*). Then, spots with the highest radiation intensity were identified, and those with similar intensities were selected as the locations for vials.

3.4.1 Preparation of samples with a target concentration of suspensions

Different concentrations of the primary PS sample (0.30 mg/mL, 0.35 mg/mL, 0.40 mg/mL, and 0.45 mg/mL) were prepared and analyzed with a UV-Vis spectroscopy to measure the intensity of the UV absorption of the samples at 365 nm wavelength (i.e., the peak relative intensity in the UVA domain of the UV lamp used in the experiment). The sample at 0.45 mg/mL PS had the closest UV absorption intensity (0.49) to 0.5, which corresponded to approx. 30% transmittance, suggesting most photons were absorbed by the suspension. Therefore, all samples were made with this concentration (0.45 mg/mL) for the UV-aging test.

3.4.2 Preparation of Test Vials

Four experimental conditions were included in the UV chamber. The vials with specific constituents were provided for primary PS and secondary PS samples in the experiment. Table 1 shows the different types of vials prepared for the experiment for each plastic type.

Table 1 – The types of vials provided for primary PS and secondary PS samples.

Material Type	Vial Type
Primary PS	UV- Heat Primary PS
	Dark-Heat Primary PS
	Dark-Cold Primary PS
Secondary PS	UV- Heat Secondary PS
	Dark-Heat Secondary PS
	Dark-Cold Secondary PS
Control	T-MQW and C-MQW

Two vials were filled with MQW (8 mL); one of these vials (T-MQW) was used to monitor the PS suspension's temperature during the exposure duration, while the second one (C-MQW) was employed as a blank. The UV-Heat primary PS and UV-Heat secondary PS were filled with 8 mL samples with a determined concentration (0.45 mg/mL). To investigate the impacts of heat on the aging of plastics, the Dark-Heat primary PS and Dark-Heat secondary PS vials were filled with the samples and covered with aluminum foil to protect the vials' contents against UV light. Furthermore, the Dark-Cold primary PS and Dark-Cold secondary PS vials were filled with plastic samples, covered with aluminum foil, and stored in the refrigerator to prevent exposure to UV light and heat.

3.4.3 Control Measurements

Samples were exposed to UV light and heat for entire Five days. During UV exposure tests, the T-MQW vial temperature was monitored daily (average temperature of 51.6 ± 0.5 ℃). Additionally, the temperature and radiation intensity at a reference position were measured before and during the UV experiment to monitor the stability of the UV lamp's irradiation intensity

throughout the experiment. Fluctuations in intensity over the course of exposures were ~ 3% (569 ± 15.8 μW/cm^2).

3.5 Characterization of Prepared Polystyrene Plastics Particles

Both primary and secondary PS samples were characterized in terms of chemical composition, morphology, particle size, and surface charge.

3.5.1 Characterization of the Chemical Composition of Prepared Plastic Particles

The chemical composition of particles was analyzed utilizing Fourier transform infrared spectroscopy (FTIR) (*Nicolet 8700, Thermo Fisher*). This analytical technique provides valuable information about the molecular composition (i.e., identification of the functional group such as-OH, -CH_3, and -C=O, in the molecules of the analyzed material) and was useful for distinguishing polymers' oxidation changes during the experiments. Dried plastic particles were required for the FTIR instrument. Hence, 8 mL of each prepared plastic suspension (~ 0.45 mg/mL) was freeze-dried (*LABCONCO, Free Zone. 2.5*), corresponding to ~ 3.6 mg dried plastic. Then, a pellet was formed from the dried powder sample and analyzed. Collected spectra from samples were compared to the PS pellets received from the manufacturer as a reference for chemical changes during experiments.

3.5.2 Morphology of the plastic particles

The morphology of the prepared plastics was observed using scanning electron microscopy (SEM, *Hitachi-S4800*). A droplet (50 μL) of each plastic suspension was air-dried individually on a stub covered with a glass slide. Then, the samples were coated with a thin layer (7.3 nm) of Au/Pd using a sputter coater under Argon gas (*Leica ACE600 Carbon/Metal coater*).

3.5.3 Identification of Particle Size and Particle Size Distribution

The particle size distribution of the plastic particles was measured by several techniques, including optical microscopy for preliminary measurements, dynamic light scattering (DLS) (*Zetasizer nano series, Malvern Panalytic*) employed for the size measurement of nanoparticles, and laser diffraction (*Malvern Matersizer 3000*) and Coulter counter (*Beckman Coulter, Multisizer 4e*) used for understanding the size of the micron-sized particles.

The preliminary size measurements of the prepared samples were completed by taking pictures from particles using an optical microscope (*Fisher Science, LAXCO L3000*) equipped with a digital camera (*LAXCO, SeBaCam Digital camera*). Samples were prepared by pipetting ~ 50 µL of the suspension onto a glass slide and covering it with a slipcover. A 10× magnitude lens was used to take ~ 30 images from each sample. The images were analyzed by processing ImageJ software to get the sample particles' average size.

DLS and laser diffraction techniques used light scattering principles to measure the particle size distributions from concentrated suspensions. Prior to running the tests, samples were ultrasonicated (*Fisher Scientific, Branson 5800*) (15 min) and mixed by a vortex mixer (*Fisher Scientific, Fisher brand*) for a few seconds. Based on the results obtained while running the tests, they were diluted if required.

In addition, the Coulter counter technique was employed to understand the size distribution of the prepared MPs. The sample was prepared by adding several drops of a particle suspension, ranging from 4 to 40 drops depending on its concentration, into 20 mL of the isotone electrolyte (NaCl). Samples were analyzed using a 100 µm aperture, and calculation was done from 2.07 µm to 60.00 µm.

3.5.4 Surface charge of the plastic particles

The surface charge of the prepared plastic particles was identified by measuring their zeta potential (*Malvern Zetasizer ZS nano*). The same suspension was placed in a folded capillary cell (*Malvern, Zetasizer Nano Series*) to get measurements of electrophoretic mobility and ZP.

Chapter 4: Results and discussion

4.1 Primary Polystyrene Plastic Particles

4.1.1 Production of Primary Plastic Particles

Suspensions of PS particles were made via anti-solvent precipitation. The impacts of several variables on the particle size were investigated, including 1) the concentration of PVA (surfactant), 2) the needle size, and 3) the injection rate. Preliminary data of mean particle sizes were obtained using an optical microscope which prevented the observation which prevented the observation of particles less than around a micrometer due to the optical limitations and diffraction limit of visible light.

To determine the effect of PVA concentration on particle formation, three different concentrations of PVA solutions (i.e., 0.1%, 1%, and 10%) were used while other variables were held constant. The higher concentration of PVA solution (10%) resulted in particles with an average diameter of 7,600 ± 3,700 nm (n = 903) as measured via an optical microscope. Those produced with lower concentrations of PVA, i.e., 0.1%, and 1%, had 22,600 ± 11,400 nm (n = 104), and 9,700 ± 7,300 nm (n = 84) mean particle size, respectively. Table 2 shows the mean particle size (mean diameter) and the number of analyzed particles of the samples produced with the different concentrations of PVA solution. This finding also can be observed in Fig. 5 which shows the images of the observed particles of each sample via the optical microscope using the ×10 magnification. Image (a) is the picture of the sample made with 0.1% PVA solution and images (b) and (c) show the particles of the samples produced with 1% and 10% PVA solutions, respectively. The amount of the particles of samples formed with 0.1% and 1% PVA solution were

smaller than the sample with 10% PVA and the size of them, especially in the sample with 0.1% PVA solution looks larger than those in the sample produced with 10% PVA solution.

The concentration of the PVA had a noticeable impact on the number of formed particles. However, its effects on the particle size are not clear by using the optical microscopy technique due to the limitations of this to observe the smaller particles. In general, there is a decreasing trend in the particle size by increasing the concentration of the PVA solution in the samples. Increasing PVA concentration enhances the viscosity of the anti-solvent solution, and thus it was important to balance between particle stabilization and preventing the suspension system from stirring properly, which is an important factor in forming small particles [21, 61, 100]. As a result, the 10% PVA solution was selected for experiments moving forward.

Table 2 – The comparative table of the samples' particle sizes using different concentrations of PVA solution.

PVA Wt%	PVA Volume (mL)	PS Concentration (mg/mL)	PS Volume (mL)	Injection Rate (mL/min)	Stirring Rate (rpm)	Needle Size (G)	Mean Diameter (nm)	Number
0.1	60	20	2	0.5	650	23	22,600 ± 11,400	104
1	60	20	2	0.5	650	23	9,700 ± 7,300	84
10	60	20	2	0.5	650	23	7,600 ± 3,700	903

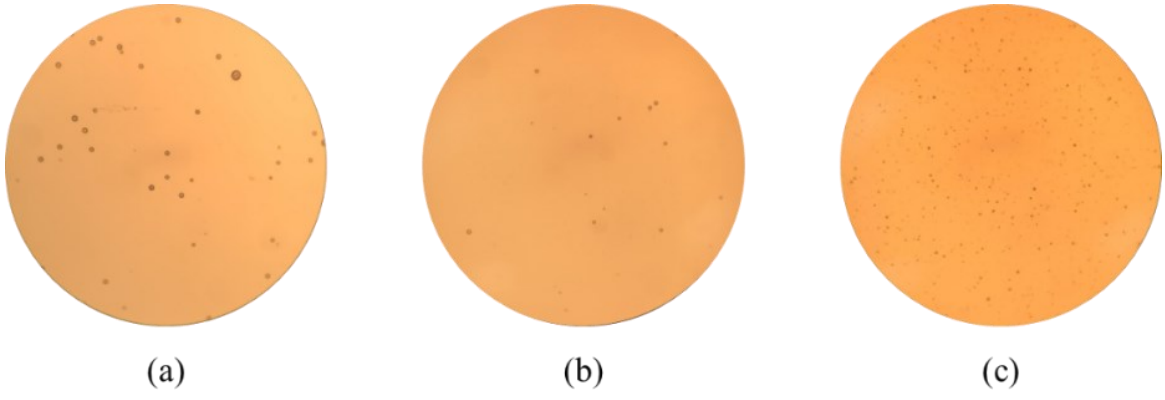

Fig. 5 – The images of the synthesized PS particle samples by different concentrations of PVA solution at ×10 magnification. (a), (b) and (c) were produced with 0.1%, 1%, and 10% PVA solutions, respectively.

The impact of the needle size on the particle size was another investigated variable by employing three different needle sizes (23, 18, and 12 G) to prepare the samples, while other variables were consistent. It can be said that the needle size was not an effective variable in the particle size of these samples. The mean particle size of the samples synthesized with the 23, 18, and 12 G needle sizes were 7,600 ± 3,700 nm, 7,100 ± 3,600 nm, and 7,000 ± 3,800 nm, respectively, as shown in Table 3. In general, the differences among the mean particle size of the samples were not insignificant, but they showed a slightly decreasing trend. It can be because of the increase in the PS solution's flow rate, which may have caused greater dispersal of PS before the anti-solvent led to phase change. While these changes were not significant, the 12 G needle was used going forward based on the decreasing trend.

Table 3 – The comparative table of the samples' mean particle sizes using different needle sizes.

PVA Wt%	PVA Volume (mL)	PS Concentration (mg/mL)	PS Volume (mL)	Injection Rate (mL/min)	Stirring Rate (rpm)	Needle Size (G)	Mean Diameter (nm)	Number
10	60	20	2	0.5	650	23	7,600 ± 3,700	903
10	60	20	2	0.5	650	18	7,100 ± 3,600	2,223
10	60	20	2	0.5	650	12	7,000 ± 3,800	1,192

Finally, different injection rates (0.25, 0.50, 2.60 mL/min) were employed to introduce the PS solution into the anti-solvent to determine the target rate while other variables were consistent for all samples. Table 4 shows the mean particle size of the samples prepared with different injection rates. Increasing the injection rate did not significantly impact the mean particle size of the samples, although a slight decreasing trend can be seen for those made with quicker injection (2.60 mL/min). The obtained result matches the findings of Vu et al. (2021) [101]. When the PS solution was introduced into the anti-solvent with the high injection rate, this quick PS

introduction can alter the local PS concentration in the anti-solvent and assist in reaching the supersaturation condition, which is essential for exceeding the equilibrium solubility and producing the very small nuclei in the larger amount. The high number of nuclei can limit the growth phase due to the lack of available PS to be consumed for growing.

Table 4 – The comparative table of samples' particle sizes using different injection rates.

PVA Wt%	PVA Volume (mL)	PS Concentration (mg/mL)	PS Volume (mL)	Injection Rate (mL/min)	Stirring Rate (rpm)	Needle Size (G)	Mean Diameter (nm)	Number
10	60	20	2	0.10	650	12	7,000 ± 3,700	827
10	60	20	2	0.25	650	12	7,700 ± 4,100	1,333
10	60	20	2	2.60	650	12	6,300 ± 2,900	2,692
10	60	20	2	one shot	650	12	6,700 ± 3,500	1,299

As mentioned above, other factors, including PS concentration, PS to PVA solution ratio, temperature, and stirring rate were kept constant for all experiments. The PS concentration was not changed because reducing the amount of the polymer in the system generally decreases the experiment yields regardless of the particle's diameter size, and the increase in PS concentration results in two unfavorable possible scenarios in which the final product can have either large particles or smaller particles with smaller particle yield [74]. There are two possible reasons for the first scenario (i.e., the production of the bigger particles): the first one is the entanglement of the polymer chain (i.e., entanglement theory) in a system with a high amount of polymer, and the second reason is that the increase in the number of PS can cause the production of larger particles and the reduction of nucleation rate in the system [74, 102]. Increasing the amount of polymer can increase the supersaturation rate and, consequently, the enhancement in the growth rate with the cost of nucleation consumption [74]. In the second scenario (the production of the smaller particles with less particle concentration), the nucleation rate can increase by enhancing the concentration

of the polymer, which leads to a decrease in the growth phase. However, the increase in nucleation rate can cause aggregation due to the fusion of several particles and reduction of particle yield [74]. These reasons also can be applied to the change in the ratio of the polymer solution to the anti-solvent solution. The temperature was held constant to prevent the prepared plastic particles from melting. Also, it may increase the particles' size [102]. The stirring rate of the experiment (320 rpm) was the closest rate to the reported stirring rate (1,000 rpm) in the previous studies to produce nanoplastics [21, 57, 61, 74]. The Beakers filled with samples were stable on the hotplate stirrer applying the employed stirring rate. Therefore, that was the maximum possible stirring rate to apply. Table 5 shows the selected values moving forward for producing each batch of primary PS plastic.

Table 5 – The table of the final selected values for each variable used to make a sample of the primary PS samples. After finalizing the value of each variable, the rest of the samples were fabricated by introducing (2.6 mL/min) of 20 mg/mL of PS solution into the anti-solvent solution.

PVA Wt%	PVA Volume (mL)	PS Concentration (mg/mL)	PS Volume (mL)	Injection Rate (mL/min)	Stirring Rate (rpm)	Needle Size (G)
10	300	20	10	2.6	320	12

Then, the heterogeneous primary PS samples produced by the determined variables were analyzed using Coulter counter to identify their mean particle size. Fig. 6a displays the particle size distribution graph of the sample using Coulter counter. Because this technique measures particle size equal to or larger than 2,000 nm, the plotted graph did not show the normal distribution (i.e., the graph did not appear bell-curve). It means that the achieved results were not accurate since only a part of the particles were analyzed. Therefore, in the next step, the sample was analyzed by Mastersizer, which works based on the laser diffraction technique, to determine

the particle size distribution more accurately (Fig. 6b, d). The mean particle size of the sample was calculated based on the 3 replications of the volume-weighted analysis, the Dv50 (i.e., the sample's particles with the same size as the median or smaller than that providing 50% of the solid volume in the suspension) was 6,410 ± 20 nm (Fig. 6b). However, the number-weighted analysis of the sample (Dn50, which is 50% of the particles at or below the median) was 330 ± 2 nm (Fig. 6d). The particles with bigger sizes possess the larger surface area causing the larger scattered lights, so due to higher light intensity, the particle size distribution based on the volume appears bigger sizes than number-weighted measurements. Nevertheless, both analysis types indicated the broad particle size range in the suspension from nanometer to micrometer. However, 90% of the particles in the sample were equal to or smaller than 595 ± 10 nm (Table 6). It confirms that although the heterogeneous sample is polydisperse, its particles were mostly in the nano-size regime. Also, the existence of a particle population in the micro-size region can be because of the aggregation of multiple particles or the passage of large particles through the filters [74]. The heterogeneous primary samples later were used to prepare the MPs primary, NPs primary, and the aged primary (UV-heat primary) samples.

Table 6 – Summarized data regarding particle size and ZP of produced plastics obtained by using Mastersizer and DLS.

Plastic type	Volume weighted diameter (nm)			Number weighted diameter (nm)			Z-Ave (nm)	PDI	ZP (mV)
	Dv10	Dv50	Dv90	Dn10	Dn50	Dn90			
Primary Heterogeneous	2,750 ± 59	6,410 ± 20	13,000 ± 140	233 ± 1	330 ± 2	595 ± 10	n/a	n/a	n/a
Primary MPs	3,500 ± 3	7,440 ± 5	13,800 ± 26	236 ± 1	340 ± 2	623 ± 5	n/a	n/a	n/a
Primary NPs	n/a	n/a	n/a	n/a	n/a	n/a	556.3 ± 9.0	0.2	- 11.9 ± 0.4
UV-Heat Primary	3,370 ± 1	7,370 ± 5	14,200 ± 30	344 ± 0	480 ± 0	899 ± 0	n/a	n/a	- 21.6 ± 0.6
Secondary MPs	3,560 ± 20	14,700 ± 291	74,500 ± 2,790	1,520 ± 0	2,280 ± 0	4,560 ± 11	n/a	n/a	n/a
Secondary NPs	n/a	n/a	n/a	n/a	n/a	n/a	155.7 ± 1.5	0.1	-45.3 ± 1.1
UV-Heat Secondary	n/a	n/a	n/a	n/a	n/a	n/a	109.0 ± 1.0	0.2	- 48.8 ± 2.7
Dark-Heat Secondary	n/a	n/a	n/a	n/a	n/a	n/a	141.4 ± 1.6	0.1	- 51.2 ± 2.6

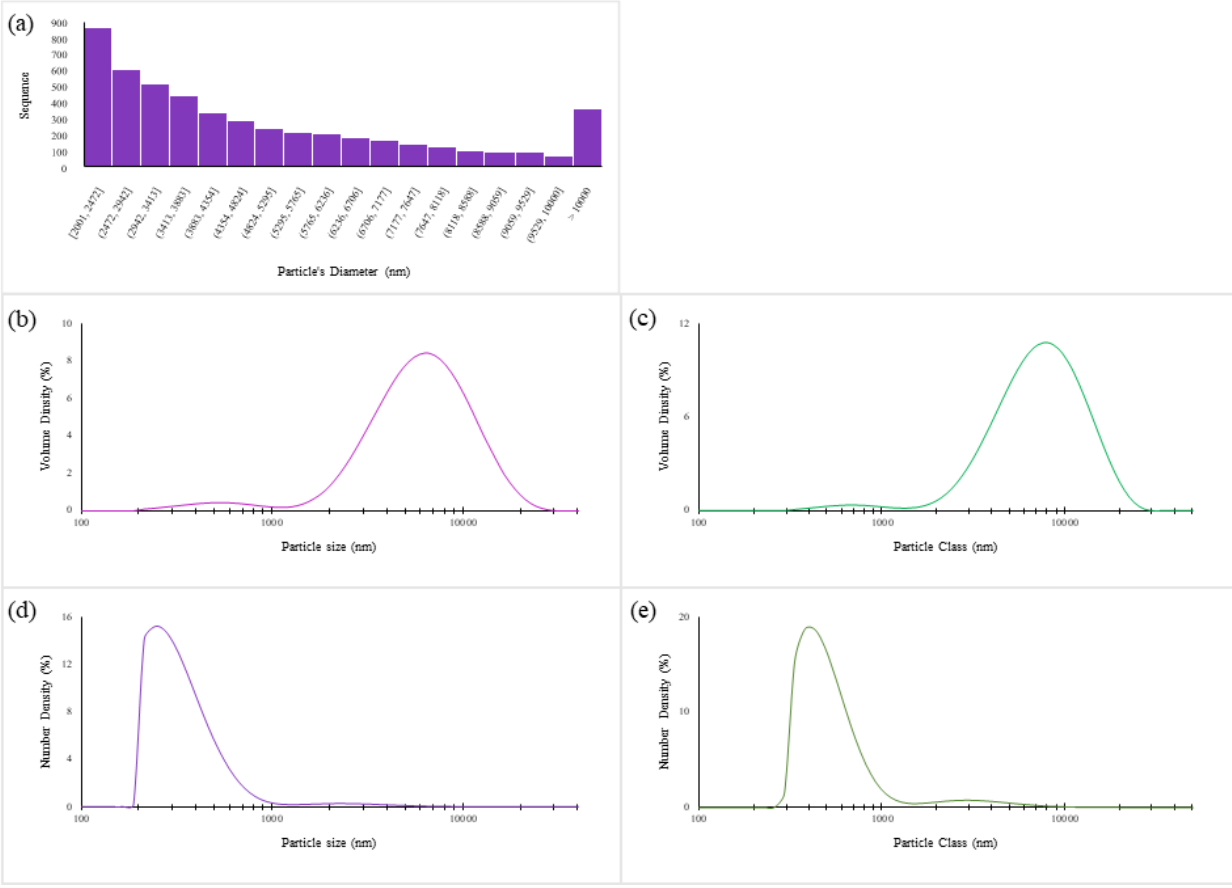

Fig. 6 – The particle size distribution graphs of the heterogeneous primary PS and UV-Heat primary PS samples using Coulter counter and Mastersizer. (a) is the particle size distribution graph of the heterogeneous primary PS obtained by Coulter counter, and the volume-weighted, (b and c), and number-weighted (d and e) are their Mastersizer analyses. Note: The scale in (a) differs from the rest of the figure.

To prepare the MPs samples the heterogeneous samples were filtered alternating with 10 µm and 5 µm filters. The mean size of the suspension's 16,922 particles (d_{50}) was 4,700 nm using Coulter counter (Table 6). Since this test did not analyze particles with sizes smaller than 2,000 nm (Fig. 7a), the sample was analyzed by Mastersizer as well. Most scattering is the result of bigger particles, which were in the micro-size region (a major peak) measured by the volume-

weighted analysis (Fig. 7b), but the number-weighted analysis reveals that most particles were in the nano-size regime (Fig. 7c).

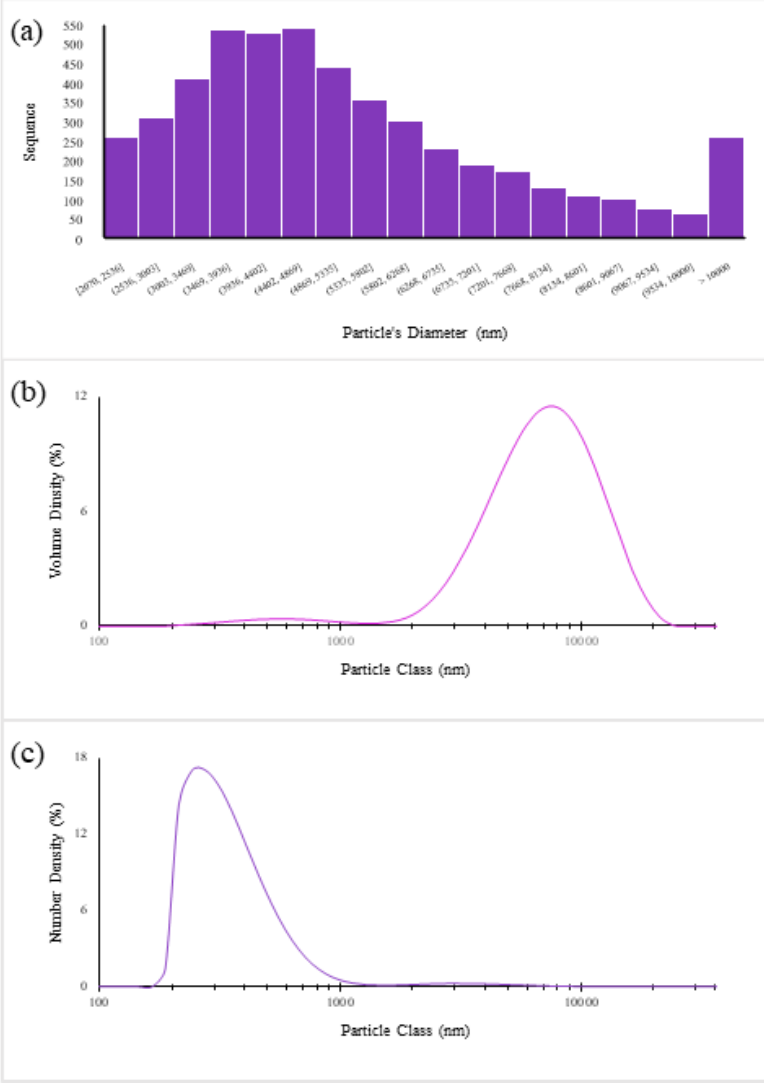

Fig. 7 – The particle size distribution of the primary MPs using Coulter counter (a) and Mastersizer (b and c). Note: The scale in (a) differs from the rest of the figure.

The volume-weighted median (Dv50) and number-weighted median (Dn50) of the suspension were 7,440 ± 5 nm and 340 ± 2 nm, respectively, (Table 6). Also, 90% of the particles had a

diameter smaller than or equal to 623 ± 5 nm (Dn90), which means that the sample's particles' sizes are mainly in the nano-size region. Based on the number-weighted results, some particles with a size bigger than 10,000 nm were not removed from the suspension by the 10 μm filter. It can be because of the pore size distribution of the filter. Moreover, the existence of particles with a smaller size than 5,000 nm in the suspension can be due to the blockage of some filter's pores or the aggregation of the smaller particles. Therefore, a close look at the size distribution of the heterogeneous primary PS and primary MPs samples indicates that vacuum filtration between 5 μm and 10 μm filters did not significantly affect the particle size distribution of the primary MPs sample.

Comparison of both techniques' data (i.e., the Coulter counter and Mastersizer) indicates that they are complementary to each other. The Coulter counter genuinely counts the particles passing through its aperture due to changes in the signals produced by momentary changes of the electrical repulsion, but detection is limited to micron-sized particles which affects the overall mean size and the particle size distribution provided by Coulter counter. The Mastersizer analyzed a broader range, from nano-size to micro-size particles and detects the intensity of the light scattered (photons) by particles, and then fits the data to calculate the particle size. Therefore, it is important to consider their differences in their principles and their limitations (i.e., the capability to measure a specific particle size range).

Given the heterogeneous mixtures produced by the anti-solvent precipitation method, the nano-size portion of the primary PS particles (the primary NPs sample) was isolated and measured using the DLS technique. The Zetasizer instrument detects and analyzes the changes in scattered light intensity due to Brownian motion. The sample's Z-average diameter was 556.3 ± 9.0 nm

with a polydispersity index of 0.2 (Table 6). The results were achieved through 3 replications (Records 1, 2, and 3) for both intensity-weighted and number-weighted analyses (Fig. 8).

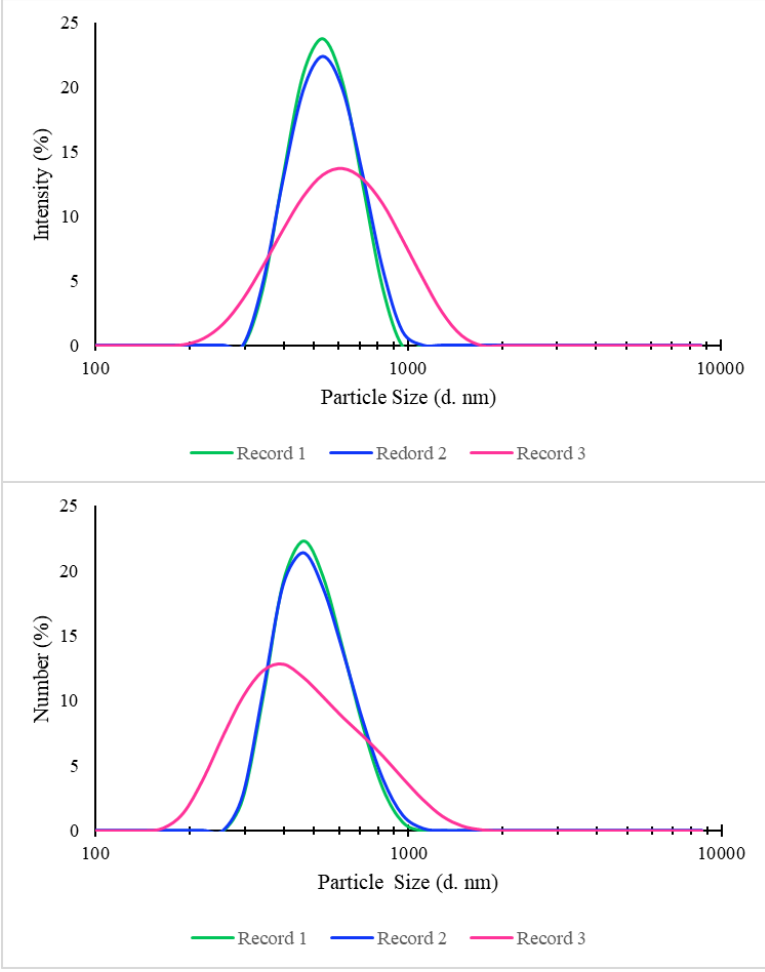

Fig. 8 – The particle size distribution graphs of the primary NPs sample using the intensity-weighted (top) and the number-weighted (bottom) analyses of DLS.

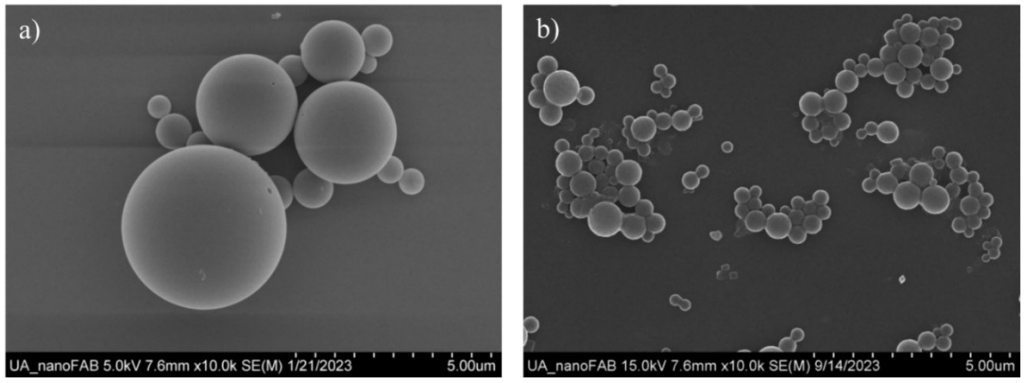

Fig. 9 – The SEM images of the primary PS sample at 5.0 kV and 15.0 kV magnification. a) imaging the primary MPs sample, b) imaging the primary NPs sample.

The next step of the sample characterization was the primary PS particles' morphology using the SEM technique. Fig. 9a and b show SEM images of the primary MPs and the primary NPs. The particles of the primary MPs sample were spherical-shaped with a smooth surface (Fig. 9a). The primary NPs sample included spherical particles in the nano-size range (Fig. 9b). Their morphology confirmed suggested they were not aged, which was later supported by FTIR analysis. In SEM images, particles appeared to be clumped together; this is likely an artifact of drying in which the reduction in solvent volume induced aggregation (Ma et al., 2005). Although it is possible that some aggregation occurred in the suspension, DLS for the primary NPs sample (Fig 8) did not indicate the presence of large aggregates of approximately 5 μm observed in the SEM (Fig. 9b).

Another important characterization of plastic particles is their surface charge, indicated by ZP. The ZP of the primary NPs suspension was – 11.9 ± 0.4 mV (Table 6). It showed that the particles had a moderately negative charge, suggesting some electrostatic repulsion with each other, although suspensions are only considered "stable" at ZP values greater than ± 30 mV [103].

In the last step of characterization, the chemical composition of the primary sample was studied. Chemical analysis by FTIR confirmed that the composition of PS was not changed from the ordered stock during the preparation process. Samples were scanned from 650 – 4,000 cm^{-1}, and the spectra of both the manufactured PS pellet and primary PS sample match the library reference (Sprouse Polystyrene by ATR or Transmission) for PS (92.73%, match with polystyrene and 96.67%, match with polystyrene, respectively). No additional peaks were observed in the primary PS sample that would suggest chemical modification during anti-solvent precipitation.

FTIR provides information on chemical bonds and functional groups in the sample's composition. However, it is important to mention that it is a semi-quantitative technique, used to observe the addition or changes in peaks due to production or aging procedures. Fig. 10 shows the FTIR spectra of the PS pellet (the green spectrum) and the primary PS sample (the purple spectrum), including their peaks' wavenumbers. Table 7 indicates the primary PS peak wavelength numbers and their respective functional groups.

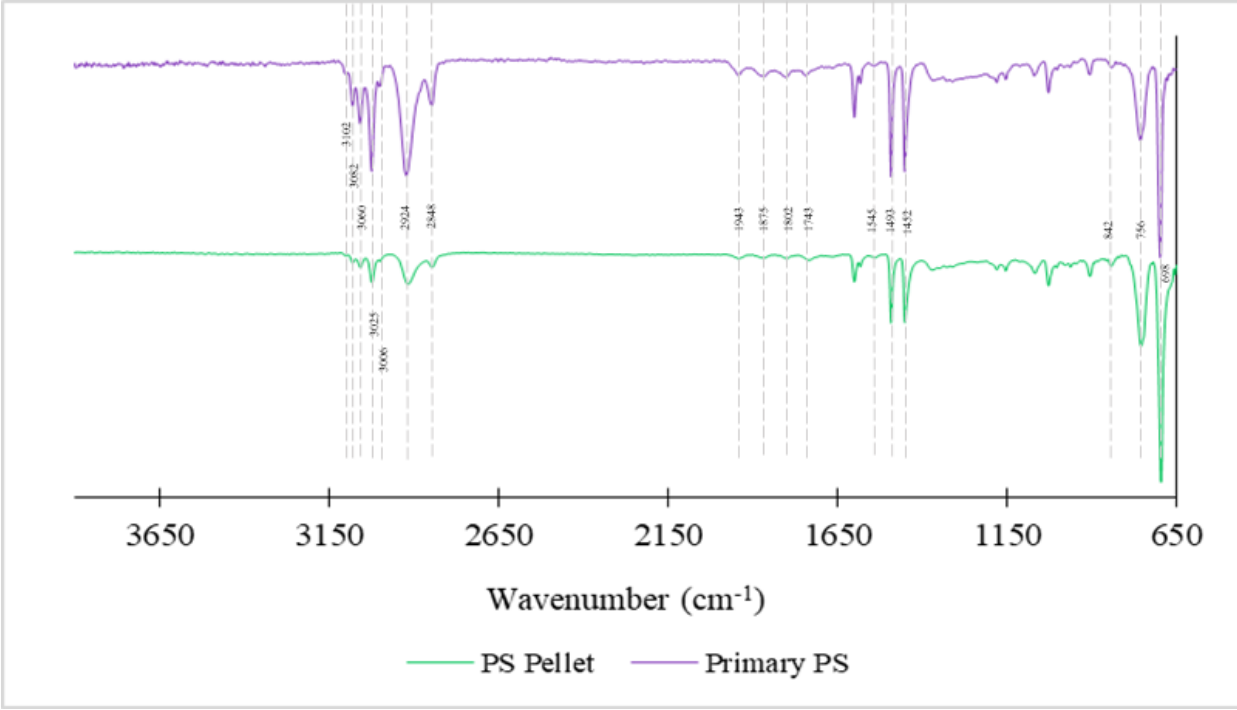

Fig. 10 – The FTIR spectrums of the primary PS sample (purple, top) and a PS pellet (green, bottom) and peak wavenumbers, see Table 7 for the corresponding functional group.

Table 7 – The table of the heterogeneous primary PS peaks and their corresponding functional groups.

Peak(s) Wavenumber(s) (cm^{-1})	Functional Group(s)	Reference(s)
698	Aromatic C-H out-of-plane bending	[8, 101, 104]
756	Aromatic in-phase H wag or aromatic C-H bond stretching	[8, 101]
842	C=C band bending	[8, 105]
1452, 1493, 1545	-CH_2 bending and aromatic ring stretching or aromatic C=C stretching	[8, 104, 106]
1601	Aromatic C=C stretching, or C-C benzene ring stretching	[101, 104, 106]
1743, 1802, 1875, 1943	Benzene's fingers	[107]
2848, 2948, 3006, 3026, 3060, 3082, 3102	Aromatic C-H stretching	[8, 16, 101, 106]

Peaks around 698 cm^{-1} in the primary PS spectrum correspond to the aromatic C-H out-of-plane bending vibration [8, 101, 104]. The peak at 756 cm^{-1} was formed by the aromatic C-H bond stretching and aromatic in-phase hydrogen wag [8, 101]. The peak at 842 cm^{-1} can be due to the vibrations of the C=C bond bending [8, 82]. The peaks at 1,452 cm^{-1}, 1,493 cm^{-1}, and 1,545 cm^{-1} refer to -CH_2 bending and aromatic ring stretching vibrations or aromatic C=C stretching [8, 104, 106]. The peak of the aromatic C=C stretching and C-C of benzene ring stretching of vinyl group

vibration is 1,601 cm^{-1} [101, 104, 106]. The benzene fingers' peaks appeared from 1,743 cm^{-1} to 1,943 cm^{-1} [107]. The peaks of the aromatic C-H stretching were displayed from 2,848 cm^{-1} to 3,102 cm^{-1} [8, 15, 101, 106]. The peaks of these functional groups are shown in the PS pellet FTIR spectrum with slight shifting (between 2 to 5 cm^{-1}). Generally, the primary PS sample's spectrum includes basic peaks related to PS plastics and is highly similar to the PS pellet's spectrum.

4.2 Secondary Polystyrene Plastic Particles

4.2.1 Production of Secondary Plastic Particles

Suspensions of secondary MPs were isolated following ball mill ground and filtered to less than 10 and 5 μm. Analysis of particle size distribution by Coulter counter indicated some particles with sizes between ~ 6,000 to ~ 8,000 nm, but most particles in the suspension had a particle size less than ~ 5,000 nm (Fig. 11a), with particles with size around 2,000 – 3,000 nm comprising the largest population. The shape of the distribution in Fig. 11a is due to the limitations of Coulter counter, which has a lower limit of detection of ~ 2,000 nm with the 100 μm aperture used here. Considering the technique's limitation, 15,632 particles of the sample were analyzed, and the median of their particle size was 2,600 nm (Table 6).

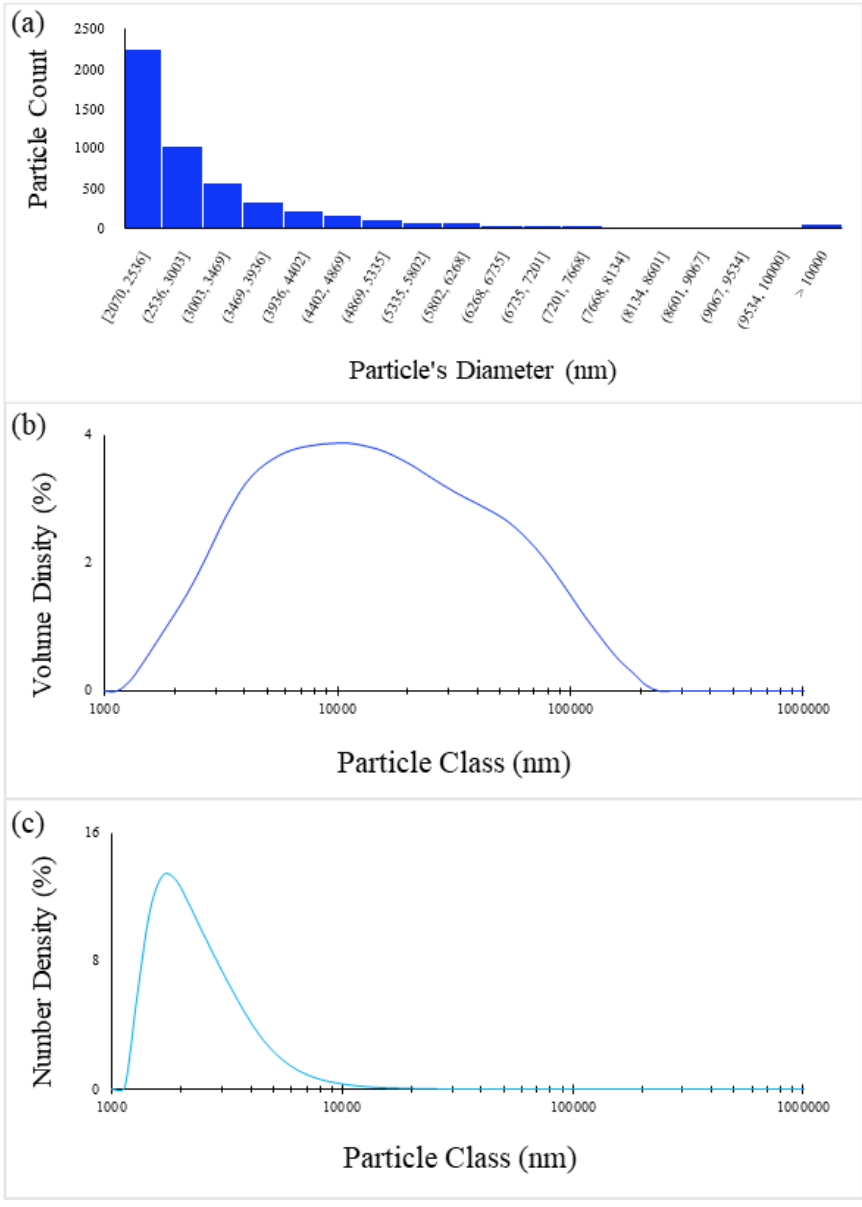

Fig. 11 – The particle size distribution of secondary MPs using Coulter counter (a) and the volume-weighted (b) and number-weighted analyses of Mastersizer (c). Note: The scale in (a) differs from the rest of the figure.

Given this limitation, samples were also analyzed via laser diffraction (Fig. 12a and b). The particle size distribution plotted as the volume-weighted data calculated that the particle size range of the suspension was in the micro-size (1,280 – 211,000 nm), but the plotted graph with the number-weighted analysis indicates that the particle size of the suspension was from 1,130 to

35,300 nm. This discrepancy is expected for suspensions with some degree of heterogeneity. The bigger particles which contain most of the particle volume in the sample will scatter the most light and skew results towards larger sizes. Accounting for this, the number-weighted results present the distribution on a weighted basis to illustrate that the majority of the particles exist at smaller sizes, agreeing with Coulter counter data. Table 6 includes the D-values of the sample of the secondary MPs sample in which the differences between using the volume-weighted and number-weighted analyses are further illustrated.

The Dv10 of the sample was 3,560 ± 20 nm, while the number-weighted one (Dn10) was 1,520 nm, which means that 10% of particles that participated in the analysis (particle count) were smaller than or equal to Dn10. The median value of the number-weighted analysis (Dn50) reveals that half of the particles in the sample were ~ 2,280 ± 0 nm. The Dv50 (14,700 ± 291 nm) compared to Dn50 shows even more significant differences. It suggests the presence of a considerable number of particles in the sample were smaller than or equal to Dn50, but the intensity of the scattered light by bigger particles was higher. Ninety percent of particles in the suspension were smaller than or equal to 4,560 ± 11 nm (Dn90).

After identifying the particle size distribution of the micro-sized portion of the secondary sample, the nano-sized part (secondary NPs) was isolated and characterized. The secondary NPs sample was prepared by differential sedimentation, 0.8 μm filtration, and concentration of the filtrate (the secondary NPs sample). Then, the particle size distribution of the secondary NPs sample was measured using the DLS technique. The Z-average of the sample was 155.7 ± 1.5 nm with a high average uniformity (PDI) of 0.1 (Table 6).

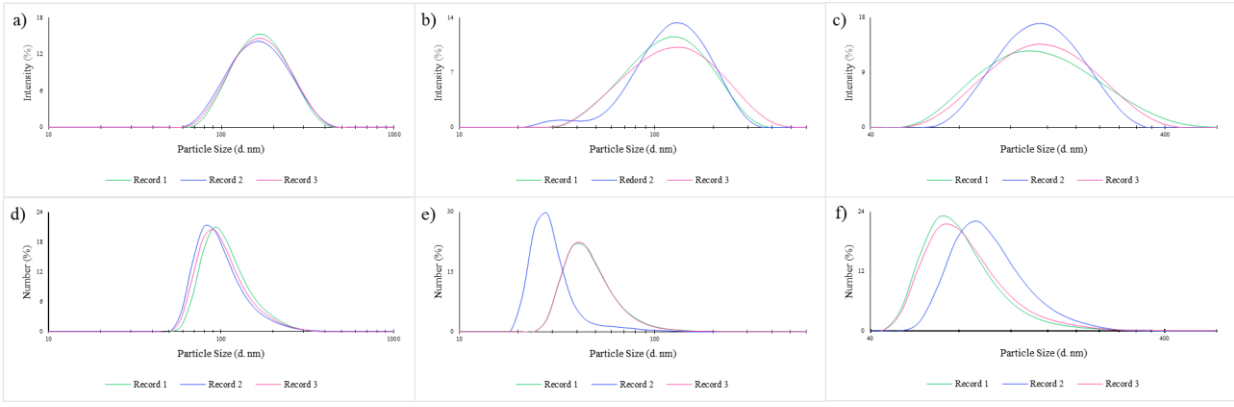

Fig. 12 – The graphs of the particle size distribution of secondary NPs (a and d), UV-Heat secondary PS (b, e), and Dark-Heat secondary PS (c, f) using the intensity-weighted (top) and number-weighted (bottom) analyses of DLS.

After identifying the particle size distribution, the morphology of the secondary PS samples (MPs and NPs) was investigated using SEM. The irregular shape of both types of secondary PS samples and their rough surface indicate their aging (Fig. 13a and b). The size differences of the samples are also obvious in the images.

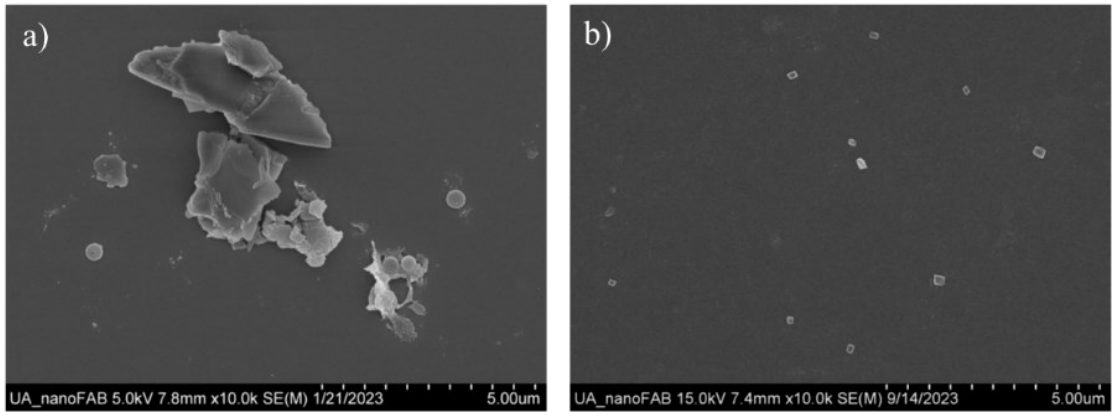

Fig. 13 – The SEM images of the secondary samples. (a) imaging of the secondary MPs under 5.0 kV magnification and (b) imaging of the secondary NPs at 15.0 kV magnification.

The ZP of the particles in the secondary NPs sample was measured using the Zetasizer technique. The sample was prepared in the same way that the primary NPs were prepared for this technique. The ZP value for the sample was – 45.3 ± 1.1 mV (Table 6). The strongly negative value of the ZP means that the particles in the suspension had a net negative charge on their surface, which made an electrostatic repulsion among particles with the negative charge. It can help to stabilize suspension by decreasing the possibility of aggregation. Their ZP (– 45.3 ± 1.1 mV) is much more negative than the primary NP sample's ZP (– 11.9 ± 0.4 mV) suggesting the chemical modifications to the secondary sample's surface.

Then, the sample was analyzed via FTIR and compared with the PS pellet's spectrum to investigate any changes (i.e., oxidations) in its composition (Fig. 14). The spectrum of secondary PS shows the peaks of the functional groups in PS (Table 8), which were discussed for the primary PS sample (91.10% match with polystyrene, HR Nicolet Sampler Library). However, presenting some new bonds and overwhelming some peaks confirm the oxidation of the plastic. The summary of the wavenumbers of the discussed peaks with respective functional groups is shown in Table 8.

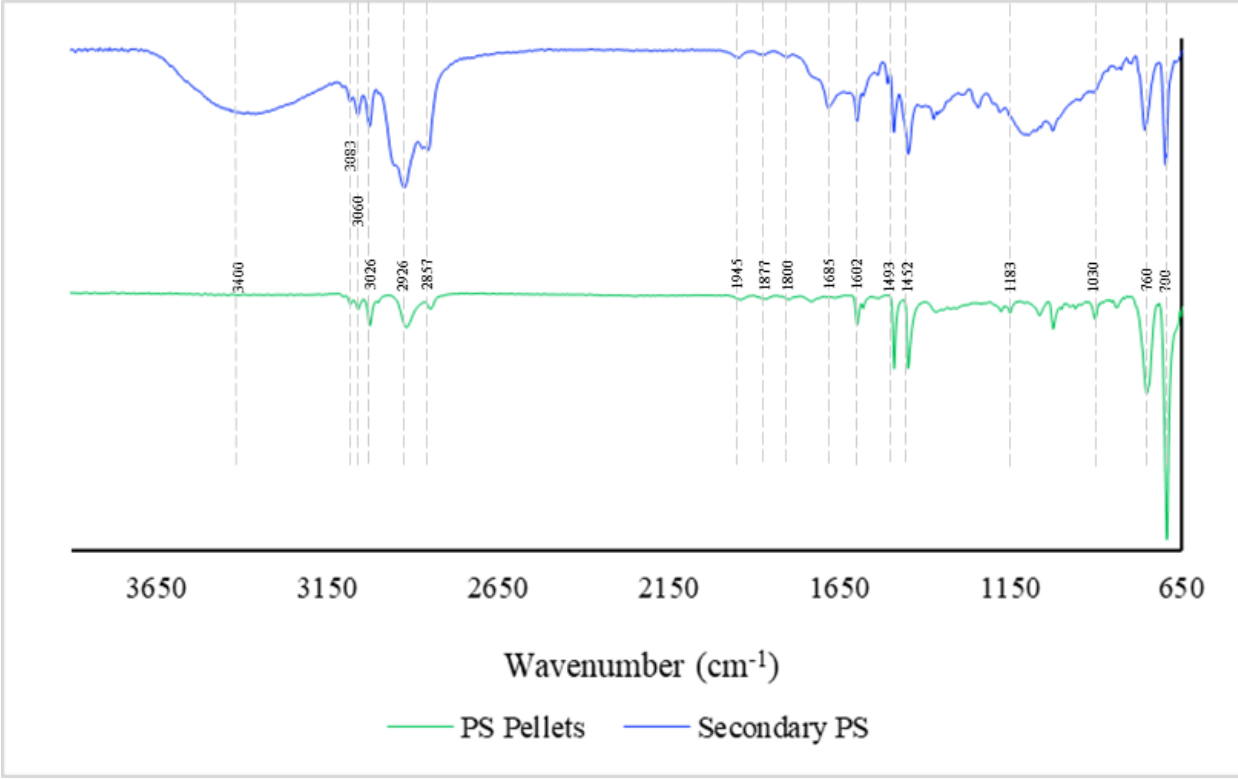

Fig. 14 – The FTIR spectra of a PS pellet (green, bottom) and secondary PS sample (blue, top), and peaks wavenumbers, see Table 8 for the corresponding functional groups.

Table 8 – The table of the secondary PS peaks' values and their corresponding functional groups.

Peak(s) Wavenumber(s) (cm^{-1})	Functional Group(s)	Reference(s)
700	Aromatic C-H out-of-plane bending	[8, 101, 104]
760	Aromatic in-phase H wag or aromatic C-H bond stretching	[8, 101]
1030	C-O (alkoxy group) stretching	[15, 106]
1183	C-O-C (ether group) stretching	[16]
1452, 1493	$-CH_2$ bending and aromatic ring stretching, or aromatic C=C stretching	[8, 104, 106]
1602	C=O (carbonyl group)	[8]
1685	C=O (carboxyl group) stretching	[106, 108]
1800, 1877, 1945	Benzene's fingers	[107]
3400	O-H (hydroxyl group) stretching	[15, 109]

The peaks observed at 1,030 cm^{-1} and 1,183 cm^{-1} are due to the C-O stretching and C-O-C stretching, respectively [15, 16, 106]. The peak at 1,685 cm^{-1} and 1,685 cm^{-1} represents the C=O (carbonyl group) bond stretching [8, 106, 108]. Also, the O-H (hydroxyl group) stretching peak appeared at 3,400 cm^{-1} with shifting to smaller wavelengths [16, 109]. The functional groups

containing oxygen can be explained by the reaction of plastic particles with oxygen during mechanical abrasion by the increasing temperature; the temperature enhancement provides the energy required for the oxidation reaction. For example, this energy was consumed to break the C-H bond; the radicals reacted with present oxygen and produced the alkoxy groups (i.e., C-O). The same explanation can be worked for forming the ether groups (i.e., the C-H bond of the aromatic ring in the PS backbone was oxidized, and the C-O-C group was formed). In addition, after C-O radical formation, the radicals can react with present hydrogen to produce C-O-O-H groups (hydroperoxide groups). The further reactions lead to the formation of C=O and C-OH [15, 108].

The comparison of the two spectra (i.e., the PS pellet and secondary PS samples) indicates that some of the main peaks of PS, which appeared in the PS pellet FTIR spectrum, underwent oxidation reaction with the present oxygen during mechanical abrasion and shearing. The peaks corresponding to the functional groups containing oxygen, such as C-O, -OH, and C=O, confirm this fact. In addition, one of the peaks (1,743 cm^{-1}) of the benzene fingers was overwhelmed.

4.3 The Exposed Primary and Secondary Polystyrene Plastic Particles to UV light and Heat

4.3.1 Production of the aged Primary PS (UV-Heat Primary PS sample) and Secondary PS (UV-Heat Secondary PS and Dark-Heat Secondary PS samples)

The prepared primary heterogeneous PS and secondary NPs samples were used as the initial samples to prepare the aged samples. All for this experiment were aged by a combination of UV light and heat. However, some secondary samples were additionally exposed only to heat under dark conditions. Aged samples were characterized to identify the differences from their unaged counterparts. The aging process impacted the plastics in different ways, including changing color reducing the particle size, and modifying their composition. Visually, the aging process caused the discoloration in the aged secondary by turning from white color to yellow color (Fig. 15). secondary PS suspensions kept under dark, cold conditions (Fig. 15, vial 2) did not change color, remaining white throughout the experiment. However, the color of the aged secondary samples - both Dark-Heat secondary PS (vial 3) and UV-Heat secondary PS (vial 4) turned to different shades of yellow. The color of the UV-Heat secondary PS sample was more intense yellow than the Dark-Heat secondary PS sample's color. Interestingly, the color of the prepared primary samples, unaged samples, and aged samples, did not change, remaining white throughout the aging experiment (not shown).

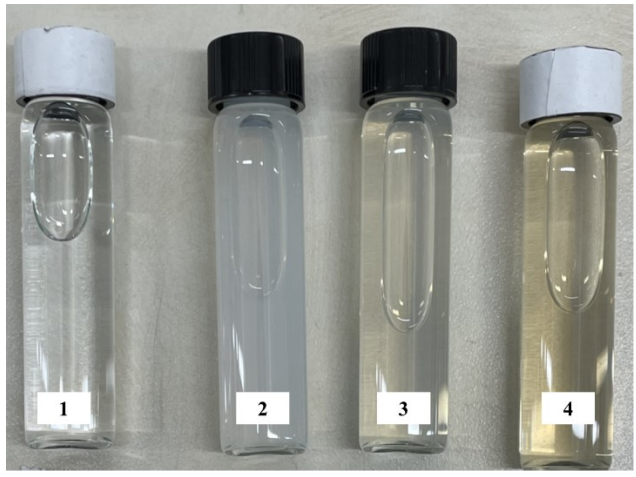

Fig. 15 – The secondary PS samples after aging test by the UV light and heat. Vials 1, 2, 3, and 4 are the blank sample, Dark-Cold secondary PS sample, Dark-Heat secondary PS, and UV-Heat secondary PS sample, respectively. The color of the sample in vials 3 and 4 was discolored and turned yellow after the aging process.

The size of the plastic particles can change due to the oxidation during aging process. Therefore, identifying the particle size of the aged samples was the first step of its characterization. Due to the existence of a few particles in micro-sizes, the particle size of the primary aged sample was measured by Mastersizer. The aged sample included two main particle size distributions at 380 nm and 2,932 nm (Fig. 6e). The number-weighted median diameter of the suspension (Dn50) was 480 ± 0 nm and its volume-weighted median (Dv50) was 7,370 ± 5 nm (Table 6). SEM images indicate that most plastic particles in the suspensions were broken down into smaller fragments due to exposure to the combination of light and heat when compared to the dark-cold control (Fig. 16a).

The particle size of the UV-Heat secondary sample was measured using DLS (Fig. 12b, and e). Prior to aging, the Z-average of the unaged secondary sample was 155.7 ± 1.5 nm, but it decreased to 109.0 ± 1.0 nm in the UV-Heat secondary sample (Table 6). Similar to the aged primary sample, particles in the aged secondary suspension were fractured into smaller pieces, resulting in particle

size distributions in the tens of nanometers). This was also confirmed later by the SEM images (Fig. 16b).

Even when the unaged secondary sample was exposed to heat and shear stresses for aging, degradation was observed (Fig. 12c and f), and most particles were broken down into smaller fragments with a smaller size (Z-average = 141.4 ± 1.6 nm) than the unaged secondary sample (Table 6). The number-weighted analysis indicates that the suspension had a large number of particles at 68.1 nm (records 1 and 3 in Fig. 12f) and 91.3 nm (record 2 in Fig. 12f).

The particle size distribution differences between the two types of aged secondary samples suggest that the extent of sample degradation from unaged secondary was less intense when only heat was applied and more intense when aged with the combination of UV light and heat (Table 6).

For all aged primary and aged secondary samples, SEM indicated irregularly shaped morphologies (Fig. 16a and b). Comparing the morphology of the plastics before the aging test (the spherical unaged primary and secondary, Fig. 9 and Fig. 13) and after ageing (the irregular-shaped aged primary and secondary samples, Fig. 16a b) the physical degradation of the plastic particles resulting in smaller fragments.

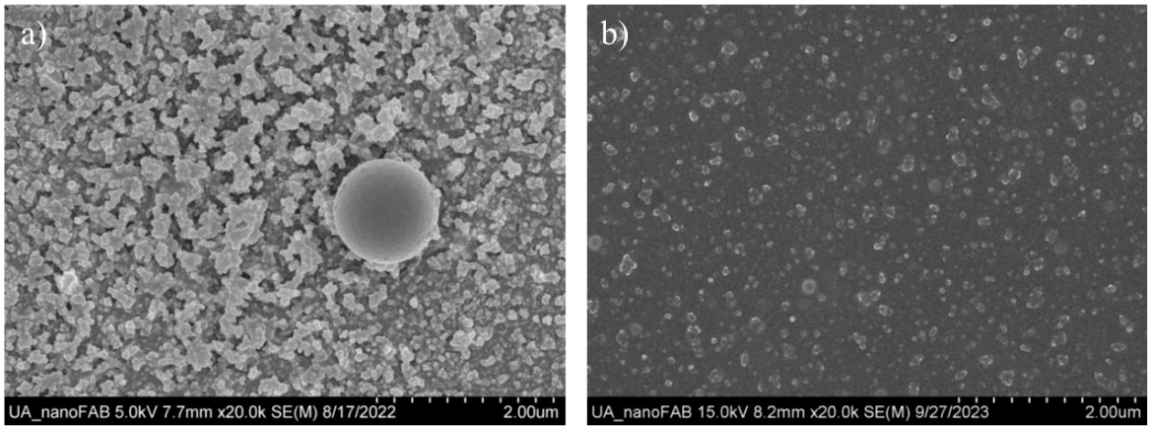

Fig. 16 – The SEM images of aged PS samples. a) imaging of UV-Heat primary PS at 5.0 kV magnification and, b) imaging of UV-Heat secondary PS at 15.0 kV magnification.

Following the morphology investigation, the surface charge of the aged samples was examined. The ZP of the UV-Heat primary PS was – 21.6 ± 0.6 mV, which was a bit more negative than the ZP of the primary PS. UV-Heat secondary PS and Dark-Heat secondary PS samples were - 48.3 ± 2.7 mV and - 51.2 ± 2.7 mV (Table 6), respectively. Both of these are slightly greater than the unaged secondary PS (– 45.3 ± 1.1 mV), indicating a strong negative charge on the particles' surface, electrostatic repulsion between the suspension's particles, and consequently a high dispersion stability.

In the last step of the characterization, the chemical analysis of the samples was performed via FTIR. The freeze-dried water controls (C-MQW samples) in both exposure tests did not result in any sample being analyzed by FTIR. The spectrum of the UV-Heat primary sample confirmed the oxidation of aged particles (89.65% match with polystyrene atactic, Hemmel Polymer and Additives). As shown in Fig. 17, the peak at 1029 cm^{-1} is attributed to the C-O bond stretching with a small shift [16, 106]. The oxidation of the C-H bond may produce the peroxyl group under UV light and heat [15, 110]. The presence of peaks at 1330 cm^{-1} and 1384 cm^{-1} can be because of

the phenolic O-H bending [15, 16]. After the breakage of the C-H bond, it reacted with oxygen and then with hydrogen [15, 16]. The carbonyl (C=O stretching) peak appeared at 1601 cm^{-1} and 1,717 cm^{-1} [8, 9, 104]. The formation of the C=O group may be started by decomposing the C-H bond and reaction with oxygen; then, the further decomposition reactions of the product lead to the formation of C=O groups [15, 110]. The bond at 3417 cm^{-1} resulted from the vibration of the O-H (hydroxyl) bond stretching [16, 109].

Comparing the spectrum of the primary PS (the heterogeneous primary PS) and UV-Heat primary sample reveals that one of the peaks (1,743 cm^{-1}) of benzene fingers was overwhelmed. In addition, a bond related to the hydroxyl group appeared after oxidation by UV light and heat. Moreover, the peaks corresponding to C=O and C-O groups were not present for unaged samples. Table 9 shows the respective functional groups of FTIR peaks of the UV-Heat primary PS sample.

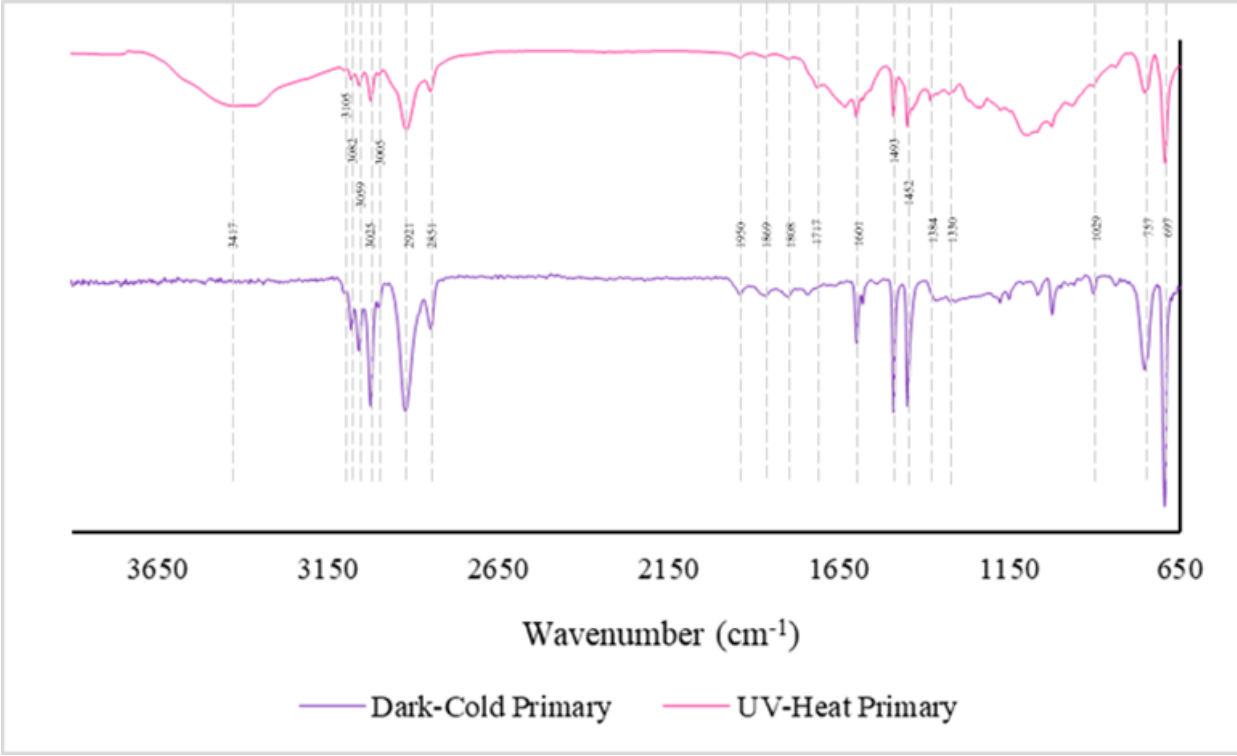

Fig. 17 – The FTIR spectra of primary PS (purple, bottom) and UV-Heat primary PS (pink, top), and peaks wavenumbers, see Table 9 for the corresponding functional groups.

Table 9 – The FTIR peaks and the corresponding functional groups of the UV-Heat primary PS sample.

Peak(s) Wavenumber(s) (cm^{-1})	**Functional Group(s)**	**Reference(s)**
697	Aromatic C-H out-of-plane bending	[8, 101, 104]
757	Aromatic in-phase H wag or Aromatic C-H bond stretching	[8, 101]
1029	C-O (alkoxy group) stretching	[15, 106]
1330, 1384	Phenolic hydroxyl C-OH bond	[15]
1452, 1493	$-CH_2$ bending and aromatic ring stretching, or aromatic C=C stretching	[8, 104, 106]
1601	C=O (carbonyl group)	[8]
1717	C=O (carbonyl group) band stretching	[8, 9, 104]
1808, 1869, 1950	Benzene's fingers	[107]
2851, 2921, 3059, 3082, 3105	Aromatic C-H stretching	[8, 16, 101, 106]
3417	O-H (hydroxyl group) stretching	[15, 109]

Studying the chemical composition of the UV-Heat secondary PS confirmed further aging compared to secondary PS (Dark-Cold secondary) (Fig. 18). The UV-Heat secondary sample's spectrum included the more intense oxidation bands compared to unaged secondary PS. All the benzene fingers peaks were overwhelmed in the spectrum of the UV-Heat secondary sample. Table 10 displays the wavenumbers of FTIR peaks and their corresponding functional groups of the UV-Heat secondary PS sample. The peak at 1027 cm^{-1} suggests the C-O bond stretching [16, 106]. The phenolic hydroxyl vibration formed a peak at 1,378 cm^{-1} [15, 16]. Peaks appeared at 1,599 cm^{-1} and 1,709 cm^{-1} because of the carbonyl group [8, 16, 106]. It may be produced by the oxidation of the C-H bond [15, 110]. The hydroxyl (O-H) stretching bond is at 3,371 cm^{-1}, with some shifting to the higher wavelength numbers [16, 109]. The formation mechanism can be explained by the same mechanism assumed for the peak at 1,378 cm^{-1} [15, 110].

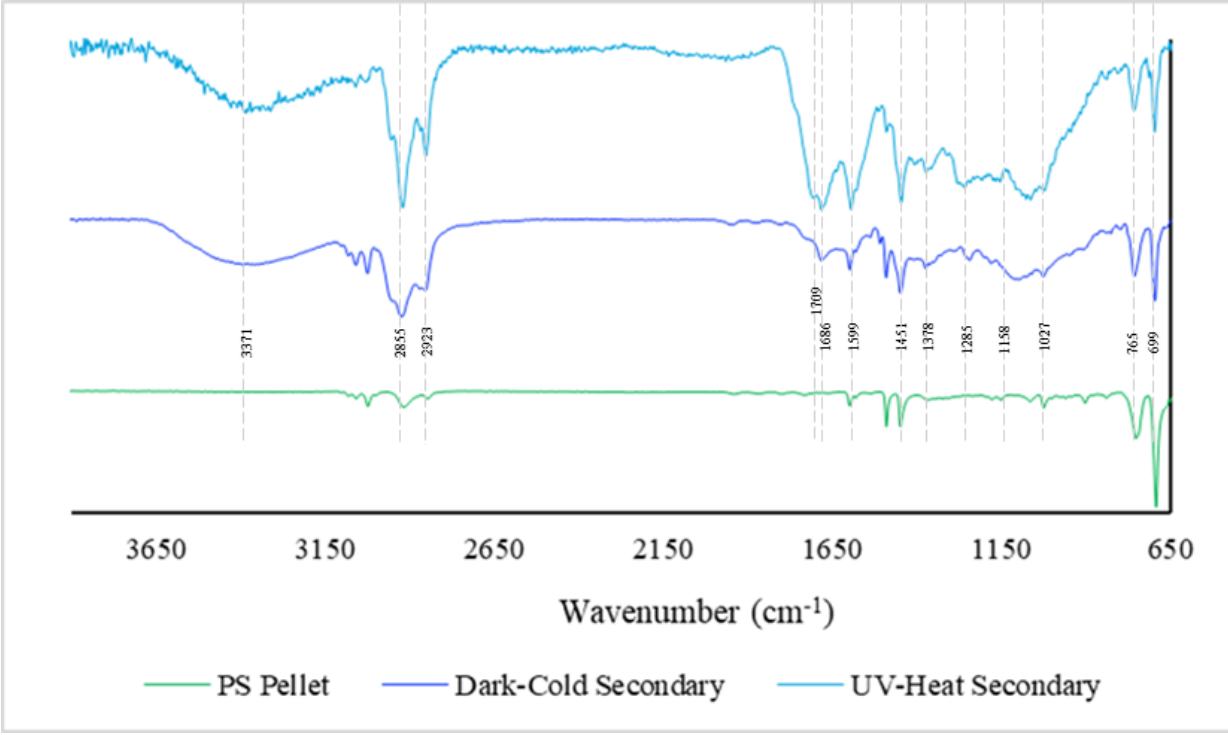

Fig. 18 – The FTIR spectra of PS pellet (green) and Dark-Cold secondary PS, i.e., secondary PS (dark blue) and UV-Heat secondary PS (light blue), and peaks wavenumbers, see Table 10 for the corresponding functional groups.

Table 10 – The FTIR peaks and the corresponding functional groups of UV-Heat secondary PS.

Peak(s) Wavenumber(s) (cm^{-1})	Functional Group(s)	Reference(s)
700	Aromatic C-H out-of-plane bending	[8, 101, 104]
765	Aromatic in-phase H wag or Aromatic C-H bond stretching	[8, 101]
1027	C-O (alkoxy group) stretching	[15, 106]
1285	CH_2 bending	[106]
1378	Phenolic hydroxyl C-OH	[15]
1451,	Aromatic C=C stretching	[104, 106]
1599, 1709	C=O (carbonyl group) band stretching	[8, 15, 106, 108]
2855, 2923	Aromatic C-H stretching	[8, 16, 101, 106]
3371	O-H (hydroxyl group) stretching	[15, 109]

The analysis of the chemical structure of the Dark-Heat secondary sample also showed some oxidized functional groups (Fig. 19). The peak at 1030 cm^{-1} can be referred to as C-O stretching [16, 106]. The peaks at 1600 cm^{-1} and 1,685 cm^{-1} were formed by the vibrations of C=O bonds

stretching [8, 106]. The further decompositions of the products can produce this bond resulting from oxidizing the C-H bond [15, 110]. The peak at 3401 cm^{-1} can be formed because of the O-H bond stretching [9, 82].

In addition, this spectrum confirmed increased oxidation in this sample compared to the secondary PS sample. Some oxidation is similar to UV-Heat secondary PS samples, including the presence of C-O, phenolic -OH, and C=O functional groups. However, less intense oxidation is observed compared with the sample exposed to the combination of UV light and heat. For example, two of the four peaks of benzene fingers (1,743 cm^{-1} and 1,802 cm^{-1}) disappeared due to the oxidation via heat while all 4 peaks disappeared in that region in the spectrum of the UV-Heat secondary sample. Table 11 shows the wavenumbers of FTIR peaks and their corresponding functional groups of the Dark-Heat secondary PS sample.

A direct comparison of the weathered NPs produced in this work with environmental samples is extremely difficult due to challenges in collecting and isolating environmental NPs in sufficient quantities. However, despite their larger size, we can get information from microplastics collected from environmental samples. In PSF [86, 87], Frequently, environmental MPs are irregularly shaped with discoloration causing a yellowish tint and cracks appearing on the surface. Similarly, in our study, the process of UV ageing of primary particles led to morphology changes. The spherical primary particles were transformed due to weathering into smaller, irregularly shaped particles. Even secondary NPs underwent a change in morphology following ageing of suspensions. Secondly, Dark-Heat and UV-Heat Secondary samples were observed to turn yellow, with this being more pronounced in the UV-Heat Secondary sample (Fig. 15). In comparison, no visual difference was observed in Dark-Cold Secondary samples that did not undergo any ageing. In addition to physical changes, similar chemical modifications observed in environmental

microplastics were detected in this work. The surface of MPs collected from nature has been shown to be oxidized compared to purchased samples that have not undergone environmental exposures[84, 86, 87]. Similarly, the aged samples in this study have exhibited the formation of the same carbonyl and hydroxyl functional groups that are observed in other studies. Thus, despite the absence of results in the literature for environmentally weathered PS NPs, the secondary NPs produced in this work bear the same characteristics of weathered plastics and are likely similar to PS NPs that currently exist in environmental waters.

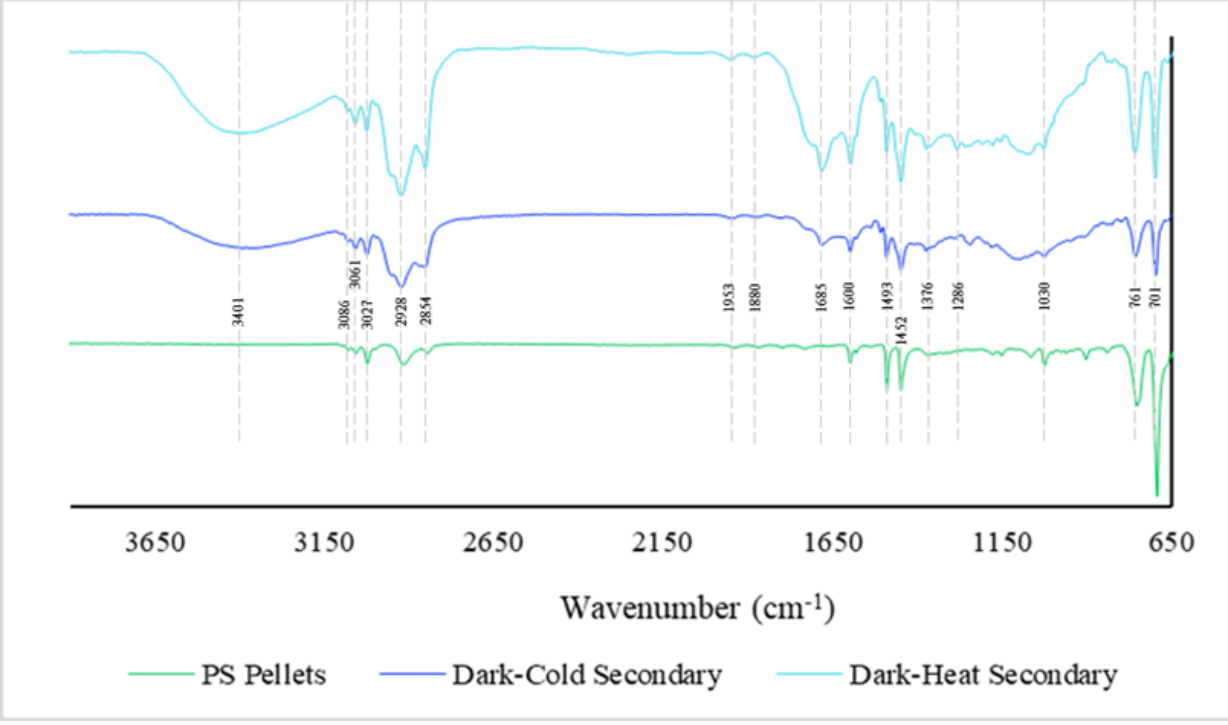

Fig. 19 – The FTIR spectra of a PS pellet (green) and Dark-Cold secondary PS, i.e., secondary PS (dark blue) and Dark-Heat secondary PS (light blue) and peaks wavenumbers, see Table 11 for the corresponding functional groups

Table 11 – The FTIR peaks and the corresponding functional groups of Dark-Heat secondary PS.

Peak(s) Wavenumber(s) (cm^{-1})	Functional Group(s)	Reference(s)
700	Aromatic C-H out-of-plane bending	[8, 101, 104]
761	Aromatic in-phase H wag or Aromatic C-H bond stretching	[8, 101]
1030	C-O (alkoxy group) stretching	[15, 106]
1286	CH_2 bending	[106]
1376	Phenolic hydroxyl C-OH	[15]
1452, 1493	-CH_2 bending and aromatic ring stretching, or aromatic C=C stretching	[8, 104, 106]
1600	C=O (carbonyl group)	[8]
1685	C=O (carbonyl group) stretching	[9, 16
1880, 1953	Benzene fingers	[107]
2854, 2925, 3061, 3086	Aromatic C-H stretching	[8, 16, 101, 106]
3401	O-H (hydroxyl group) stretching	[15, 109]

Chapter 5: Ongoing/Future Works & Conclusion

5.1 Ongoing/Future Works

Plastic pollution has received a lot of attention in the world [1]. Plastics are found in different environments, especially in aquatic ecosystems [111]. Plastic debris is degraded in the environment and fractured to MPs (1 μm to 5 mm) and NPs (< 1 μm) due to different factors, including mechanical shearing, photooxidation, and chemical oxidation [4, 18]. Micro- and nanoplastics can adversely impact organisms and microorganisms. They can enter living systems such as fish by different pathways including ingestion and accumulate in their organs [17, 18]. They also can impact bacteria by attaching to their surface and changing their behavior, such as decreasing their growth activity [26]. Therefore, many studies focus on the investigation of the impacts of MNPs on biological systems [26, 111]. Hence, the production and characterization of the plastics closely resembling the plastic particles in nature and their employment in environmental testing can provide a better understanding of plastics and their effects on the environment.

Four types of PS nanoplastics (unaged primary PS, unaged secondary PS, aged primary, and secondary PS) prepared and characterized following the procedures explained above were applied in two ongoing environmental tests. In the first, plastic suspensions introduced to an anaerobic bioreactor are investigating the changes in the microbial community, production of biogas (i.e., methane gas), and their impact on the antibiotic resistance genes in bacteria. In preliminary data (Fig. 20), increasing the concentration of the aged and unaged primary particles from 25 μm/L to 150 μm/L had the greatest impact and reduced the CH_4 gas yield. The same trend was observed for the aged and unaged secondary particles. This suggests that the existence of a high concentration of nanoplastics regardless of their aging situation, has adverse impacts on biogas

production of the bacteria as a valuable byproduct of anaerobic digestion. At 150 mg/L, secondary particles decreased CH_4 to a greater extent than primary particles. In addition, observing the impacts on bacterial antibiotic resistance genes following NP exposure indicates an increase in the antibiotic resistance condition in the microbial community in the sludge.

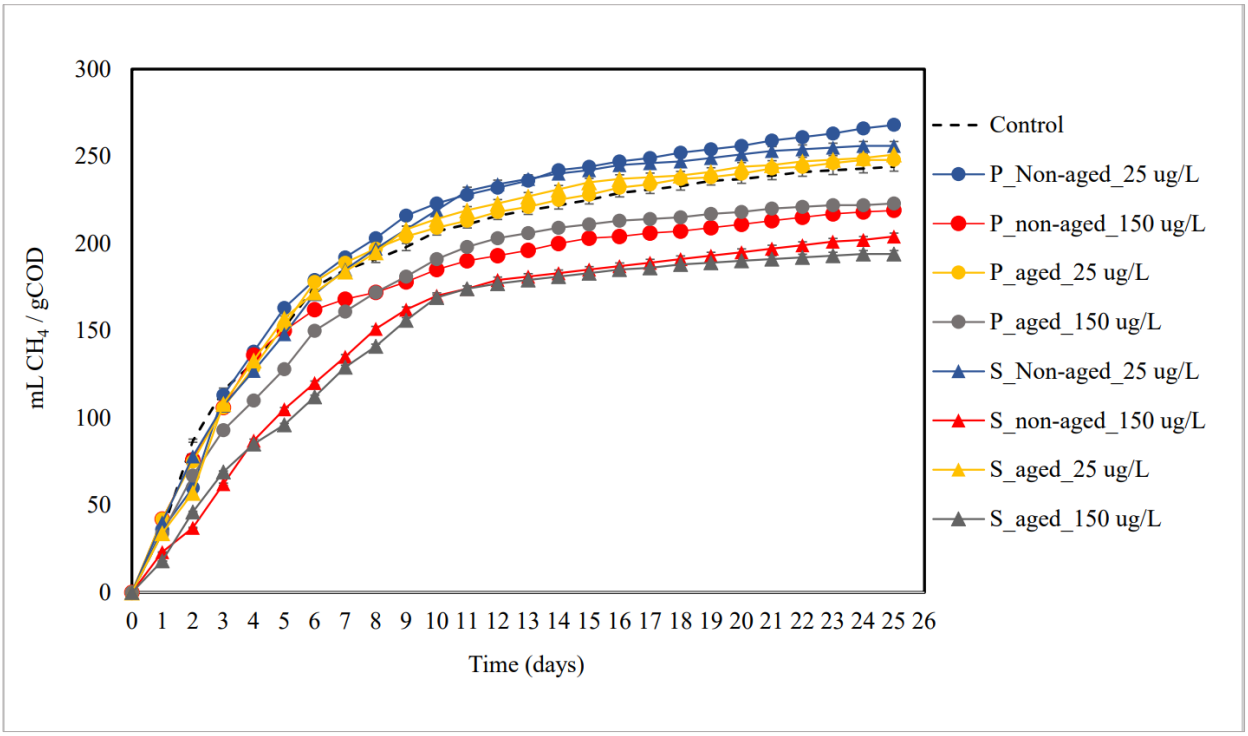

Fig. 20 – Methane production over time in anaerobic bioreactors exposed to suspensions of nanoplastics. Preliminary data.

Similarly, the impact of the weathered NPs on the digestive tract of fruit flies Drosophila melanogaster) is being investigated. The unaged primary and secondary PS described in this thesis as well as commercially purchased fluorescent PS were added to the insects' food, and their impacts on cellular communication, renewing capacity, which is crucial for health maintenance, and microbiota alterations are being studied.

In future environmental studies, including toxicology studies, the plastic particles produced by the procedures developed in this thesis can be used to more accurately investigate the impact of produced particles on biota. The same particles can be used in fate and transport testing to understand NP mobility and where NPs may accumulate in the environment. In addition, these methods can be expanded to other plastics produced with different polymers so that the impact of plastic-type can be studied.

Moreover, since the size selection step was challenging for the preparation of both MPs and NPs, it can be improved in other future works regarding the preparation of NMPs, for instance by employing dialysis, differential sedimentation, centrifugation, or recirculating filtration. It helps to prepare a more uniform particle size with a narrower distribution in samples. Also, during the production of the samples, there was a massive particle loss, so applying a filtration method with less loss will make the production method more feasible. Moreover, there is a possibility to apply the employed anti-solvent method on other types of plastics by using a proper solvent or a mixture of the solvents or changing the temperature in other future studies. However, the method used to form secondary samples should be translatable for other plastics.

5.2 Conclusion

In this study, four types of PS plastics (unaged primary and secondary and aged primary and secondary plastics) were prepared. Spherical primary NPs and MPs particles were formed from PS pellets through the anti-solvent precipitation, although the majority of the prepared suspensions had significant numbers of particles at nano-sizes. The irregular secondary MPs and NPs were created by mechanical abrasion of PS pellets. Both types of plastics were aged via UV light and heat. The aged plastics had irregular shapes. The characterization of each plastic was studied to investigate the changes made during the preparation process. All plastics had negative surface

charges; the oxidized plastics had more negative surface charges compared to primary PS. In addition, the analysis of the chemical composition of the plastics showed that the primary PS has the same chemical structure (functional groups) as PS pellets. However, the aged primary PS had some oxidized functional groups confirming its degradation. The produced secondary PS plastic was oxidized during the preparation process. It further degraded after aging, and the secondary plastic exposed to UV and heat was oxidized to a greater extent compared to those exposed to only heat.

Comparing the prepared particles in this study with the collected plastic particles debris in the environment (in other works) indicates that the formed particles' morphology and chemical composition had acceptable similarities. This assisted this study to achieve its goal, which was making particles closely resemble those in nature.

References

1. Alimi, O.S., et al., *Weathering pathways and protocols for environmentally relevant microplastics and nanoplastics: What are we missing?* Journal of Hazardous Materials, 2022. **423**: p. 126955.
2. Peng, L., et al., *Micro-and nano-plastics in marine environment: Source, distribution and threats—A review.* Science of the total environment, 2020. **698**: p. 134254.
3. Chen, Q., et al., *Enhanced uptake of BPA in the presence of nanoplastics can lead to neurotoxic effects in adult zebrafish.* Science of the Total Environment, 2017. **609**: p. 1312-1321.
4. Alimi, O.S., et al., *Microplastics and nanoplastics in aquatic environments: aggregation, deposition, and enhanced contaminant transport.* Environmental science & technology, 2018. **52**(4): p. 1704-1724.
5. Rai, P.K., et al., *Micro-and nano-plastic pollution: Behavior, microbial ecology, and remediation technologies.* Journal of cleaner production, 2021. **291**: p. 125240.
6. Cai, Z., et al., *Biological degradation of plastics and microplastics: A recent perspective on associated mechanisms and influencing factors.* Microorganisms, 2023. **11**(7): p. 1661.
7. Tsai, M.-H., et al., *Destabilization of polystyrene nanoplastics with different surface charge and particle size by Fe electrocoagulation.* Science of The Total Environment, 2023. **872**: p. 162254.
8. Hernandez, L.M., et al., *Analysis of ultraviolet and thermal degradations of four common microplastics and evidence of nanoparticle release.* Journal of Hazardous Materials Letters, 2023. **4**: p. 100078.

9. Alimi, O.S., et al., *Effects of Weathering on the Properties and Fate of Secondary Microplastics from a Polystyrene Single-Use Cup.* Journal of Hazardous Materials, 2023: p. 131855.

10. Kim, M.S., et al., *A review of biodegradable plastics: chemistry, applications, properties, and future research needs.* Chemical Reviews, 2023. **123**(16): p. 9915-9939.

11. Geyer, R., J.R. Jambeck, and K.L. Law, *Production, use, and fate of all plastics ever made.* Science advances, 2017. **3**(7): p. e1700782.

12. Bond, T., et al., *The occurrence and degradation of aquatic plastic litter based on polymer physicochemical properties: a review.* Critical reviews in environmental science and technology, 2018. **48**(7-9): p. 685-722.

13. Bergmann, M., et al., *Observations of floating anthropogenic litter in the Barents Sea and Fram Strait, Arctic.* Polar biology, 2016. **39**: p. 553-560.

14. Gigault, J., et al., *Current opinion: what is a nanoplastic?* Environmental pollution, 2018. **235**: p. 1030-1034.

15. Mao, R., et al., *Aging mechanism of microplastics with UV irradiation and its effects on the adsorption of heavy metals.* Journal of hazardous materials, 2020. **393**: p. 122515.

16. Liu, J., et al., *Aging significantly affects mobility and contaminant-mobilizing ability of nanoplastics in saturated loamy sand.* Environmental Science & Technology, 2019. **53**(10): p. 5805-5815.

17. Junaid, M., et al., *Transgenerational impacts of micro (nano) plastics in the aquatic and terrestrial environment.* Journal of Hazardous Materials, 2023. **443**: p. 130274.

18. Li, Z., et al., *Impacts of nanoplastics on bivalve: Fluorescence tracing of organ accumulation, oxidative stress and damage.* Journal of hazardous materials, 2020. **392**: p. 122418.

19. Wang, Q., et al., *Effects of bisphenol A and nanoscale and microscale polystyrene plastic exposure on particle uptake and toxicity in human Caco-2 cells.* Chemosphere, 2020. **254**: p. 126788.

20. Pitt, J.A., et al., *Uptake, tissue distribution, and toxicity of polystyrene nanoparticles in developing zebrafish (Danio rerio).* Aquatic Toxicology, 2018. **194**: p. 185-194.

21. Tanaka, K., et al., *Preparation of nanoscale particles of five major polymers as potential standards for the study of nanoplastics.* Small, 2021. **17**(49): p. 2105781.

22. Zhao, C., et al., *Particle formation mechanisms in the nanoprecipitation of polystyrene.* Langmuir, 2020. **36**(44): p. 13210-13217.

23. Zielińska, A., et al., *Polymeric nanoparticles: production, characterization, toxicology and ecotoxicology.* Molecules, 2020. **25**(16): p. 3731.

24. Modena, M.M., et al., *Nanoparticle characterization: what to measure?* Advanced Materials, 2019. **31**(32): p. 1901556.

25. Guo, X. and J. Wang, *The chemical behaviors of microplastics in marine environment: A review.* Marine pollution bulletin, 2019. **142**: p. 1-14.

26. Wang, R., et al., *Bacterial Interactions with Nanoplastics and the Environmental Effects They Cause.* Fermentation, 2023. **9**(11): p. 939.

27. Shen, M., et al., *Micro (nano) plastics: unignorable vectors for organisms.* Marine Pollution Bulletin, 2019. **139**: p. 328-331.

28. Gigault, J., et al., *Nanoplastics are neither microplastics nor engineered nanoparticles.* Nature nanotechnology, 2021. **16**(5): p. 501-507.

29. Osswald, T.A., E. Baur, and N. Rudolph, *Plastics handbook: the resource for plastics engineers*. 2019: Carl Hanser Verlag GmbH Co KG.

30. Jagtap, T.U. and H.A. Mandave, *Machining of plastics: a review.* Int J Eng Res Gen Sci, 2015. **3**(2): p. 577-581.

31. Bîrcă, A., et al., *Introduction in thermoplastic and thermosetting polymers*, in *Materials for biomedical engineering*. 2019, Elsevier. p. 1-28.

32. Cantor, K.M. and P. Watts, *Plastics materials*, in *Applied plastics engineering handbook*. 2011, Elsevier. p. 3-5.

33. Ellison, C.J., M.K. Mundra, and J.M. Torkelson, *Impacts of polystyrene molecular weight and modification to the repeat unit structure on the glass transition− nanoconfinement effect and the cooperativity length scale.* Macromolecules, 2005. **38**(5): p. 1767-1778.

34. Kik, K., B. Bukowska, and P. Sicińska, *Polystyrene nanoparticles: Sources, occurrence in the environment, distribution in tissues, accumulation and toxicity to various organisms.* Environmental Pollution, 2020. **262**: p. 114297.

35. Buchwalter, S., *Semiconductor Chip Underfill Materials.* Encyclopedia of Materials: Science and Technology, 2001: p. 8332-8335.

36. Askadskiĭ, A.A., *Computational materials science of polymers*. 2003: Cambridge Int Science Publishing.

37. Tanaka, M., et al., *Recommended table for the density of water between 0 C and 40 C based on recent experimental reports.* Metrologia, 2001. **38**(4): p. 301.

38. Collier, J.R., et al., *Elongational rheology by different methods and orientation number.* Journal of applied polymer science, 2007. **105**(6): p. 3551-3561.

39. Lane, W., *Determination of Solubility of Styrene in Water and of Water in Styrene.* Industrial & Engineering Chemistry Analytical Edition, 1946. **18**(5): p. 295-296.

40. Mitrano, D.M., P. Wick, and B. Nowack, *Placing nanoplastics in the context of global plastic pollution.* Nature Nanotechnology, 2021. **16**(5): p. 491-500.

41. Abdolahpur Monikh, F., et al., *Can current regulations account for intentionally produced nanoplastics?* Environmental Science & Technology, 2022. **56**(7): p. 3836-3839.

42. Sorensen, R.M., R.S. Kanwar, and B. Jovanovi, *Past, present, and possible future policies on plastic use in the United States, particularly microplastics and nanoplastics: A review.* Integrated Environmental Assessment and Management, 2023. **19**(2): p. 474-488.

43. Sun, H., R. Jiao, and D. Wang, *The difference of aggregation mechanism between microplastics and nanoplastics: Role of Brownian motion and structural layer force.* Environmental Pollution, 2021. **268**: p. 115942.

44. Francalanci, S., E. Paris, and L. Solari, *On the prediction of settling velocity for plastic particles of different shapes.* Environmental Pollution, 2021. **290**: p. 118068.

45. Shearer, S.A. and J.R. Hudson, *Fluid mechanics: stokes' law and viscosity.* Measurement Laboratory, 2008. **3**.

46. Suaria, G., et al., *Dynamics of transport, accumulation, and export of plastics at oceanic fronts*. 2022, Springer.

47. Jiao, R., et al., *Aggregation, settling characteristics and destabilization mechanisms of nano-particles under different conditions.* Science of The Total Environment, 2022. **827**: p. 154228.

48. Lyklema, J., H. Van Leeuwen, and M. Minor, *DLVO-theory, a dynamic re-interpretation.* Advances in colloid and interface science, 1999. **83**(1-3): p. 33-69.

49. van Oss, C.J., *The extended DLVO theory*, in *Interface Science and Technology*. 2008, Elsevier. p. 31-48.

50. *Mastersizer 3000 Customer*

Training Course. 2017; Available from: https://www.malvernpanalytical.com/en/assets/malvern%20panalytical%20-%20mastersizer%203000%20training%20materials_tcm50-97739.pdf.

51. Park, S.-J. and M.-K. Seo, *Intermolecular force.* Interface science and technology, 2011. **18**: p. 1-57.

52. Martin, L.M., et al., *Materials, surfaces, and interfacial phenomena in nanoplastics toxicology research.* Environmental Pollution, 2022. **292**: p. 118442.

53. Xie, M. and Q. He, *Solution of Smoluchowski coagulation equation for Brownian motion with TEMOM.* Particuology, 2022. **70**: p. 64-71.

54. Osinsky, A. and N. Brilliantov, *Anomalous aggregation regimes of temperature-dependent Smoluchowski equations.* Physical Review E, 2022. **105**(3): p. 034119.

55. Ulam, S., *Marian Smoluchowski and the theory of probabilities in physics.* American journal of physics, 1957. **25**(7): p. 475-481.

56. Farner, J.M., et al., *Effect of freeze/thaw on aggregation and transport of nano-TiO 2 in saturated porous media.* Environmental Science: Nano, 2020. **7**(6): p. 1781-1793.

57. Wu, C.Y. and W. Wang, *Application of antisolvent precipitation method for formulating excipient-Free nanoparticles of Psychotropic drugs.* Pharmaceutics, 2022. **14**(4): p. 819.

58. Chen, X., et al., *Preparation of cyclosporine A nanoparticles by evaporative precipitation into aqueous solution.* International journal of pharmaceutics, 2002. **242**(1-2): p. 3-14.

59. Schmid, K., C. Arpagaus, and W. Friess, *Evaluation of the Nano Spray Dryer B-90 for pharmaceutical applications.* Pharmaceutical development and technology, 2011. **16**(4): p. 287-294.

60. Thorat, A.A. and S.V. Dalvi, *Liquid antisolvent precipitation and stabilization of nanoparticles of poorly water soluble drugs in aqueous suspensions: Recent developments and future perspective.* Chemical Engineering Journal, 2012. **181**: p. 1-34.

61. Kakran, M., et al., *Preparation of nanoparticles of poorly water-soluble antioxidant curcumin by antisolvent precipitation methods.* Journal of Nanoparticle Research, 2012. **14**: p. 1-11.

62. Marqusee, J. and J. Ross, *Kinetics of phase transitions: Theory of Ostwald ripening.* The Journal of chemical physics, 1983. **79**(1): p. 373-378.

63. Jungblut, S. and C. Dellago, *Pathways to self-organization: Crystallization via nucleation and growth.* The European Physical Journal E, 2016. **39**: p. 1-38.

64. Kabalnov, A., *Ostwald ripening and related phenomena.* Journal of Dispersion Science and Technology, 2001. **22**(1): p. 1-12.

65. Yec, C.C. and H.C. Zeng, *Synthesis of complex nanomaterials via Ostwald ripening.* Journal of Materials Chemistry A, 2014. **2**(14): p. 4843-4851.

66. Nagarajan, R., *Self-assembly: from surfactants to nanoparticles*. 2019: John Wiley & Sons.

67. Miyazawa, T., et al., *A critical review of the use of surfactant-coated nanoparticles in nanomedicine and food nanotechnology.* International journal of nanomedicine, 2021: p. 3937-3999.

68. De, S., et al., *A review on natural surfactants.* RSC advances, 2015. **5**(81): p. 65757-65767.

69. Dixit, S.G., A.R. Mahadeshwar, and S.K. Haram, *Some aspects of the role of surfactants in the formation of nanoparticles.* Colloids and Surfaces A: Physicochemical and Engineering Aspects, 1998. **133**(1-2): p. 69-75.

70. Liu, Z. and L. Yang, *Antisolvent precipitation for the preparation of high polymeric procyanidin nanoparticles under ultrasonication and evaluation of their antioxidant activity in vitro.* Ultrasonics sonochemistry, 2018. **43**: p. 208-218.

71. Jia, S., et al., *Recent progress in antisolvent crystallization.* CrystEngComm, 2022. **24**(17): p. 3122-3135.

72. Callaghan, C., et al., *Cellulose Acetate Microbeads for Controlled Delivery of Essential Micronutrients.* ACS Sustainable Chemistry & Engineering, 2023. **11**(12): p. 4749-4758.

73. Zhang, B., et al., *Inverse vulcanised sulfur polymer nanoparticles prepared by antisolvent precipitation.* Journal of Materials Chemistry A, 2022. **10**(26): p. 13704-13710.

74. Tanaka, K., et al., *Size-Controlled Preparation of Polyethylene Nanoplastic Particles by Nanoprecipitation and Insights into the Underlying Mechanisms.* ACS omega, 2023. **8**(16): p. 14470-14477.

75. De Marco, I., et al., *Control of particle size, at micrometric and nanometric range, using supercritical antisolvent precipitation from solvent mixtures: Application to PVP.* Chemical Engineering Journal, 2015. **273**: p. 344-352.

76. Zhang, X., et al., *Preparation of itraconazole nanoparticles by anti-solvent precipitation method using a cascaded microfluidic device and an ultrasonic spray drier.* Chemical Engineering Journal, 2018. **334**: p. 2264-2272.

77. Yesil-Celiktas, O. and E.O. Cetin-Uyanikgil, *In vitro release kinetics of polycaprolactone encapsulated plant extract fabricated by supercritical antisolvent process and solvent evaporation method.* The Journal of Supercritical Fluids, 2012. **62**: p. 219-225.

78. Reynaud, S., et al., *Nanoplastics: From model materials to colloidal fate.* Current Opinion in Colloid & Interface Science, 2022. **57**: p. 101528.

79. Song, Y.K., et al., *Combined effects of UV exposure duration and mechanical abrasion on microplastic fragmentation by polymer type.* Environmental science & technology, 2017. **51**(8): p. 4368-4376.

80. Amobonye, A., et al., *Plastic biodegradation: Frontline microbes and their enzymes.* Science of the Total Environment, 2021. **759**: p. 143536.

81. D'Orazio, J., et al., *UV radiation and the skin.* International journal of molecular sciences, 2013. **14**(6): p. 12222-12248.

82. Ekvall, M.T., et al., *Nanoplastics formed during the mechanical breakdown of daily-use polystyrene products.* Nanoscale advances, 2019. **1**(3): p. 1055-1061.

83. Mhiret Gela, S. and T.A. Aragaw, *Abundance and characterization of microplastics in main urban ditches across the Bahir Dar City, Ethiopia.* Frontiers in Environmental Science, 2022. **10**: p. 35.

84. Rowenczyk, L., et al., *Microstructure characterization of oceanic polyethylene debris.* Environmental science & technology, 2020. **54**(7): p. 4102-4109.

85. Ter Halle, A., et al., *To what extent are microplastics from the open ocean weathered?* Environmental Pollution, 2017. **227**: p. 167-174.

86. Battulga, B., M. Kawahigashi, and B. Oyuntsetseg, *Behavior and distribution of polystyrene foams on the shore of Tuul River in Mongolia.* Environmental Pollution, 2020. **260**: p. 113979.

87. Xie, Q., et al., *Characteristics of expanded polystyrene microplastics on island beaches in the Pearl River Estuary: abundance, size, surface texture and their metals-carrying capacity.* Ecotoxicology, 2021: p. 1-12.

88. Brignac, K.C., et al., *Marine debris polymers on main Hawaiian Island beaches, sea surface, and seafloor.* Environmental science & technology, 2019. **53**(21): p. 12218-12226.

89. Uurasjärvi, E., et al., *Microplastic concentrations, size distribution, and polymer types in the surface waters of a northern European lake.* Water Environment Research, 2020. **92**(1): p. 149-156.

90. Shi, Y., et al., *Natural weathering severity of typical coastal environment on polystyrene: Experiment and modeling.* Polymer Testing, 2019. **76**: p. 138-145.

91. Liu, L., et al., *Aggregation and deposition kinetics of polystyrene microplastics and nanoplastics in aquatic environment.* Bulletin of Environmental Contamination and Toxicology, 2021. **107**(4): p. 741-747.

92. Shams, M., I. Alam, and I. Chowdhury, *Aggregation and stability of nanoscale plastics in aquatic environment.* Water Research, 2020. **171**: p. 115401.

93. El Hadri, H., et al., *Nanoplastic from mechanically degraded primary and secondary microplastics for environmental assessments.* NanoImpact, 2020. **17**: p. 100206.

94. Astner, A., et al., *Mechanical formation of micro-and nano-plastic materials for environmental studies in agricultural ecosystems.* Science of the Total Environment, 2019. **685**: p. 1097-1106.

95. Mafla-Endara, P.M., et al., *Exposure to polystyrene nanoplastics reduces bacterial and fungal biomass in microfabricated soil models.* Science of The Total Environment, 2023. **904**: p. 166503.

96. Xiang, Y., et al., *Microplastics and environmental pollutants: key interaction and toxicology in aquatic and soil environments.* Journal of Hazardous Materials, 2022. **422**: p. 126843.

97. Amereh, F., et al., *The emerging risk of exposure to nano (micro) plastics on endocrine disturbance and reproductive toxicity: From a hypothetical scenario to a global public health challenge.* Environmental Pollution, 2020. **261**: p. 114158.

98. Ning, Q., et al., *Combined effects of nanosized polystyrene and erythromycin on bacterial growth and resistance mutations in Escherichia coli.* Journal of Hazardous Materials, 2022. **422**: p. 126858.

99. Zhang, B., et al., *Micro (nano) plastic size and concentration co-differentiate the treatment performance and toxicity mechanism in aerobic granular sludge systems.* Chemical Engineering Journal, 2023. **457**: p. 141212.

100. Kumar, R., et al., *Liquid antisolvent crystallization of pharmaceutical compounds: current status and future perspectives.* Drug Delivery and Translational Research, 2023. **13**(2): p. 400-418.

101. Vu, K.B., et al., *Polystyrene nanoparticles prepared by nanoprecipitation: A recyclable template for fabricating hollow silica.* Journal of Industrial and Engineering Chemistry, 2021. **97**: p. 307-315.

102. Kefer, S., T. Friedenauer, and H.-C. Langowski, *Characterisation of different manufactured plastic microparticles and their comparison to environmental microplastics.* Powder Technology, 2022. **412**: p. 117960.

103. 2015; Available from: https://www.research.colostate.edu/wp-content/uploads/2018/11/ZetaPotential-Introduction-in-30min-Malvern.pdf.

104. de Moraes, J.d.D.P., et al., *Investigation of the Ultraviolet Irradiation on Blend Films of PS/PCL.* European Journal of Engineering and Technology Research, 2021. **6**(2): p. 29-33.

105. *IR spectrum table & chart*. Available from: https://www.sigmaaldrich.com/CA/en/technical-documents/technical-article/analytical-chemistry/photometry-and-reflectometry/ir-spectrum-table.

106. Sharma, T. and M. Garg, *Pristine, irradiated and nanocomposite polystyrene: recent experimental and theoretical developments.* Transactions on Electrical and Electronic Materials, 2021. **22**(4): p. 394-418.

107. Smith, B., *The benzene fingers, part I: Overtone and combination bands.* Spectroscopy, 2016. **31**(7): p. 30–34-30–34.

108. Torikai, A., A. Takeuchi, and K. Fueki, *The effect of temperature on the photo-degradation of polystyrene.* Polymer degradation and stability, 1986. **14**(4): p. 367-375.

109. Chaudhary, A.K., K. Chaitanya, and R. Vijayakumar, *Synergistic effect of UV and chemical treatment on biological degradation of Polystyrene by Cephalosporium strain NCIM 1251.* Archives of Microbiology, 2021. **203**: p. 2183-2191.

110. Yousif, E. and R. Haddad, *Photodegradation and photostabilization of polymers, especially polystyrene.* SpringerPlus, 2013. **2**(1): p. 1-32.

111. Wang, L., et al., *Bacterial and fungal assemblages and functions associated with biofilms differ between diverse types of plastic debris in a freshwater system.* Environmental Research, 2021. **196**: p. 110371.

Appendix

The milling time was selected based on the temperature of the paste during the milling process to ensure that the temperature was below 30 ℃. This temperature was safe, avoiding the plastic particles melting. Table 12 shows the temperature of PS paste changes in different milling times. Based on the data, the temperature of the paste was enhanced by increasing the milling time.

Table 12 – The temperature of the PS pastes and the corresponding milling time.

Milling Time (min)	Temperature (℃)
5	22.1
8	24.9
10	27.2
13	27.9
15	28.4
18	29.4

Although the temperature at 5 and 8 min is under 30 ℃, 10 min was selected. Regardless of the paste's temperature, the longer milling time leads to the production of smaller particles. It was necessary to balance the paste's temperature, milling time, and feasibility of the methodology. Therefore, an attempt was made to keep the milling time as short as possible for the method's feasibility.

Different concentrations of the PS suspension were made and analyzed by the UV-Vis spectroscopy instrument. Table 13 shows the intensity of UV light absorption for each tested concentration.

Table 13 – The intensity of the UV light absorption of the primary PS samples with different concentrations.

Concentration (mg/mL)	Absorption
0.30	0.304
0.35	0.361
0.40	0.389
0.45	0.492

According to the UV lamp's manual, the lamp's highest relative intensity was at 365 nm in the UVA domain. Hence, the intensity of the absorption of the UV light by each sample was measured to ensure the selected concentration received high enough intensity for the aging process. The target absorbance was considered 0.5. So, the sample with the closest absorbance to the mentioned value was selected. The selected sample with a concentration of ~ 0.45 mg/mL had UV light absorption of 0.49 intensity at 365 nm, which was high enough for the experiment. Fig. 21 shows the UV light absorption intensity by the samples with different concentrations (0.30 mg/mL, 0.35 mg/mL, 0.40 mg/mL, and 0.45 mg/mL).

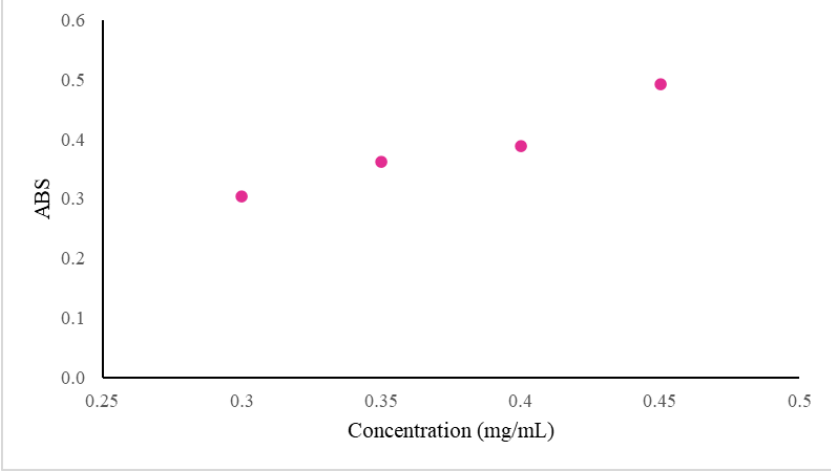

Fig. 21 – UV light absorption intensities of samples with different concentrations